Minute-scale proteomics profiling resolves the chronological mechanics of yeast cell death

Zizhuo Zhou[1,2,3], Rui Sun[1,2,3], Zhaoxing Li[1,2,3], Shuaiyao Wang[1,2,3], Liujia Qian[1,2,3], Zhenwu Dai[1,2,3], Lei Zeng[1,2,3], Kunpeng Ma[1,2,3], Guangmei Zhang[1,2,3], Tiannan Guo[1,2,3]*

[1]Affiliated Hangzhou First People's Hospital, State Key Laboratory of Medical Proteomics, School of Medicine, School of Future Biomedicine, Westlake University, Hangzhou, Zhejiang Province, China.

[2]Westlake Center for Intelligent Proteomics, Westlake Laboratory of Life Sciences and Biomedicine, Hangzhou, Zhejiang Province, China.

[3]Research Center for Industries of the Future, School of Life Sciences, Westlake University, Hangzhou, Zhejiang Province, China.

*Corresponding author: guotiannan@westlake.edu.cn

Highlights

- Minute-scale proteomics uncovers temporal trajectories of yeast cell death.
- Dynamic modeling identifies candidate drivers of stress-specific death programs.
- Acetic acid and H_2O_2 drive distinct metabolic exhaustion and genomic triage trajectories, respectively.
- Late-stage autophagy coincides with an irreversible loss of reproductive viability under acetic acid stress.

Abstract

Biological state transitions operate as continuous processes, yet are predominantly studied through discrete snapshots that obscure longitudinal dynamics. To resolve this, we monitored the proteome dynamics of *Saccharomyces cerevisiae* under lethal stress at 1-minute intervals, generating a minute-scale proteome movie whose high-temporal-resolution protein trajectories reconciled conflicting previous endpoint results by revealing sampling-time-dependent regulatory direction. Using neural ordinary differential equations and time-resolved pathway analysis, we reconstructed the proteome dynamics and identified temporally related molecular events. Acetic acid induced metabolic exhaustion through energy-expensive defense and lethal mitochondrial hyperactivation. Conversely, hydrogen peroxide triggered genomic triage, prioritizing DNA repair at the cost of organelle quality control. Interestingly, longitudinal survival validation suggests that peak autophagy coincides with the loss of reproductive viability, consistent with a late attempt to maintain immediate metabolic persistence that fails to restore cell division. Together, we characterize cell death as a set of temporally orchestrated execution programs, revealing temporal logic from adaptation to irreversible collapse. Ultimately, this study indicates that high-throughput mass spectrometry-based proteomics can construct high-resolution proteome videos, offering a new approach for resolving continuous biological state transitions.

Introduction

Biological systems operate as dynamic continua, where cellular state transitions from homeostasis to stress adaptation or death are driven by the precise temporal regulation of molecular interaction networks. Among these state transitions, the progression of how cells perceive lethal stress[1], commit to a fate[2], and ultimately execute orchestrated molecular death programs is of fundamental biological importance. Unlike accidental cell death manifesting as a chaotic and unordered cellular collapse, regulated cell death (RCD) serves as a genetically encoded and highly structured mechanism essential for maintaining population survival under severe stress[3]. The yeast *Saccharomyces cerevisiae* has

served as a premier model organism to uncover the conservation of these lethal subroutines[4]. Over the past decades, extensive research has cataloged the distinct morphological and biochemical endpoints of yeast RCD. For instance, exposure to hydrogen peroxide induces yeast apoptotic RCD (yA-RCD), displaying a phenotype characterized by severe oxidative damage[5,6] and chromatin degradation[7,8]. In contrast, the execution program triggered by high-dose acetic acid drives necrotic RCD (yN-RCD), which involves a profound trans-organelle crisis[9], severe intracellular acidification[10], and mitochondrial depolarization[11,12].

However, our understanding of these processes remains largely derived from static endpoints, leaving the continuous execution mechanics obscured. As summarized by a recent review[13], current yeast cell death related studies predominantly follow two paradigms: capturing static snapshots at predefined phenotypic endpoints (from minutes[14], hours[15] to days[16-18] post-treatment), or employing time-course designs with sparse sampling intervals[19] (45, 120, 200 minutes). While these approaches have extensively cataloged the static molecular hallmarks of yeast cell death, their coarse temporal granularity at the molecular level is fundamentally misaligned with the rapid timescale of biological signaling. Consequently, they are insufficient to capture the rapid, transient molecular decisions that define the trajectory of RCD. This limitation is particularly pronounced under acute lethal stress, where the system is pushed to its limits and simultaneously undergoes a multitude of concurrent biological activities. To fully reconstruct the trajectory of cell fate, it is imperative to move beyond static profiling toward high-temporal-resolution monitoring of proteome dynamics that captures the kinetics of the system in real-time.

Recent advances in mass spectrometry-based proteomics[20], particularly the coupling of robust sample preparation with high-throughput data-independent acquisition mass spectrometry (DIA-MS)[21], have now made it feasible to capture deep, comprehensive proteomics landscapes with the requisite throughput and reproducibility. While current DIA platforms have largely solved the data acquisition bottleneck, the dynamic inference of continuous biological processes from these high-dimensional datasets presents unresolved computational challenges. Traditional statistical methods, which rely heavily on biological replicates to assess variance[22,23], are inadequate for analyzing time-evolving trajectories characterized by non-linear dynamics and inherent stochasticity. Furthermore, conventional differential expression analyses can only identify proteins whose abundance correlates with the given perturbation, making it difficult to distinguish initial causal events from their subsequent effects. Resolving this requires advanced computational strategies capable of reconstructing continuous evolution from discrete data, thereby decoupling downstream physical consequences from the upstream regulatory signals that precede them.

To address these challenges of sparse sampling and static analytical limitations, we developed an integrated profiling and analytical strategy designed to resolve the temporal dynamics of cell fate decisions. Here, we present a minute-scale, comprehensive proteomic landscape of *S. cerevisiae* undergoing two canonical forms of regulated cell death: regulated necrosis (yN-RCD) triggered by high-dose acetic acid[24], and apoptotic cell death (yA-RCD) induced by hydrogen peroxide[5]. To capture these rapid dynamics, we coupled high-frequency sampling (1-minute intervals) with quantitative DIA-MS. The resulting data were processed through a multi-tiered analytical pipeline, progressing from unsupervised clustering to Generalized Additive Models (GAMs) for non-linear trend estimation, and ultimately to conditional latent neural ordinary differential equations (Neural ODEs) for representation learning. Using gradient-based saliency, this framework prioritized proteins whose temporal behavior most strongly shaped the model-predicted proteome trajectory, rather than simply those with the largest abundance changes. These saliency-informed trajectories nominated condition-specific candidate drivers and revealed distinct temporal programs for acetic acid and hydrogen peroxide induced cell death. Crucially, by anchoring these computationally inferred dynamics to time-resolved clonogenic survival assays, we pinpointed the irreversible "Point of No Return" under acetic acid treatment. Ultimately, this study resolves the high-resolution temporal logic

governing the transition from stress adaptation to irreversible systemic collapse. Beyond yeast cell death, the proteome video profiling established here provides an extendable approach to study other dynamic cellular processes.

Results

Minute-scale proteomic profiling of the yeast dying process

To investigate the proteome dynamics under lethal stress, we designed a high-frequency time-series proteomic experiment monitoring proteome evolution at a one-minute resolution across a continuous 100-minute window (**Fig. 1A**). We induced yN-RCD with 400 mM acetic acid and yA-RCD with 5 mM hydrogen peroxide in *S. cerevisiae* cultures, with both treatments confirmed to cause complete viability loss within the sampling period **(Supplementary note 1)**. To capture transient molecular states, biological activities were instantly quenched using trichloroacetic acid[25,26]. The raw data were acquired on two Q Exactive HF mass spectrometers using a 60-min liquid chromatography gradient and processed with DIA-NN[27], yielding a high-density dataset of 3013 high-confidence proteins across 299 samples. Rigorous quality control confirmed high reproducibility and consistent proteome depth (**Extended Fig. 1A, B**). Furthermore, principal variance component analysis following reference-material-based batch correction[28] confirmed that the biological treatment-time interaction accounted for the largest fraction of variance (24.58%) (**Extended Fig. 1C-F**).

Trajectory analysis reveals a five-stage progression of cellular collapse

To quantify the dynamic relationship between the two death modes, we calculated the Euclidean distances within the first ten principal components, visualizing the continuous temporal evolution (**Fig. 1B**). This trajectory analysis allowed us to resolve the proteome dynamics into five temporal stages, which were further corroborated by stage-specific principal component analysis snapshots (**Fig. 1C**). During the early phase (Stage One, 0 to ~20 min), pairwise distances among acetic acid, H_2O_2, and control trajectories remained minimal and non-significant (**Extended Fig. 1G**), indicating a latent window preceding the commitment to specific death subroutines. However, as stress persisted (Stage Two, ~21 - ~40 min), the system underwent a pronounced bifurcation. The pairwise distances between all groups surged significantly (Acetic acid vs H_2O_2, $P < 0.01$, **Extended Fig. 1G**), reflecting the execution of highly divergent, stress-specific programs. Following this peak divergence, the distance between two lethal trajectories contracted significantly in the intermediate phases (Stage Three and Four, ~41 - ~80 min), exhibiting non-significant statistical divergence in Stage Three ($P > 0.05$, **Extended Fig. 1G**), before exhibiting a secondary separation in the terminal phase (Stage Five, 81-100 min) (**Fig. 1C**). This complex divergence-convergence-redivergence pattern suggests that despite initiating distinct early responses, the proteomes transiently transition through a shared molecular state before ultimately rediverging into distinct terminal phenotypes.

Shared and stress-specific proteomic programs orchestrate cellular responses to lethal stress

To extract robust biological trends from high-frequency stochastic fluctuations (**Extended Fig. 2A**), we applied spectral analysis using the fast Fourier transform. By decomposing the temporal signal, we identified an optimal cutoff frequency (0.08 min^{-1}) that filtered high-frequency noise while preserving biological regulatory events (**Extended Fig. 2B**). This yielded a smoothed dataset tailored for trend analysis (**Extended Fig. 2C**) and a downsampled matrix for temporal biological events interpretation and dynamic modeling (**Extended Fig. 2D**).

Temporal clustering (maSigPro) identified distinct temporal expression patterns shared between acetic-acid-induced yN-RCD and H_2O_2-induced yA-RCD. The dominant mode (represented by Cluster 4 in **Fig. 2A**; full set in **Extended Fig. 3A**) exhibited a rapid, coordinated downregulation upon stress, featuring a transient recovery phase before terminal repression (**Fig. 2A, C**). Gene Ontology enrichment of these downregulated clusters highlighted ribosome biogenesis, RNA

processing, and translation initiation, indicating that yeast cells were undergoing a conserved growth-arrest program (**Fig. 2B, Extended Fig. 3B**) regardless of the specific death subroutine. In contrast, Cluster 3 displayed a sustained upregulation trajectory across both lethal conditions, enriched in mitochondrial respiratory chain components (**Fig. 2B, 2C, Extended Fig. 3B**). To validate the biological fidelity of our high-frequency dataset and assess the propagation of transcriptional signatures, we benchmarked our clusters against the canonical Environmental Stress Response (ESR) gene sets[29] (**Extended Fig. 3C**). Fisher's exact tests shared a significant concordance: the downregulated clusters (2, 4, 6) showed a robust intersection with ESR-repressed genes (P = 1.45E-58). This alignment supports that the biological stress signatures captured in our dataset are consistent with well-established cellular response patterns, suggesting that the transcriptional ESR is propagated to the functional proteome level under acute lethal conditions.

Complementing trajectory-based clustering, Weighted Gene Co-expression Network Analysis (WGCNA) provided a topological view of protein co-expression relationships. Module-trait relationship analysis (**Fig. 2D**) identified the turquoise module as a core homeostatic network, functionally mirroring the growth-arrest program. Its dynamics (**Fig. 2E**) was characterized by uniform suppression of translation regulators across both stress conditions. Network topology analysis (**Fig. 2G**) identified high-connectivity hubs such as Rli1, an essential iron-sulfur protein required for ribosome export and translation initiation[30,31], and Prp43, an ATP-dependent RNA helicase required for pre-mRNA splicing and the systematic disassembly of spliceosomes[32]. The central position of these hubs within the co-expression network suggests they represent structurally critical nodes within the transcription and translation machinery, whose downregulation is tightly coupled to the global system collapse. Beyond shared responses, WGCNA resolved a distinct Pink module specifically induced under acetic acid stress (**Fig. 2D, 2F**). This module comprised mitochondrial ribosome components, such as Mrpl33 and Rsm19[33] (**Fig. 2G, Extended Fig. 3G**), highlighting a condition-specific preservation and remodeling of mitochondrial translational machinery. This topological consistency suggests that the observed growth arrest is not a result of independent protein fluctuations, but rather the coordinated deactivation of a tightly coupled functional module.

High-resolution kinetics resolve intrinsic homeostatic oscillations and divergent execution landscapes of yeast cell death

While clustering analyses captured global trends, they are inherently limited in resolving individual protein dynamics and capturing non-linear temporal behaviors. More critically, traditional differential analyses typically assume a stationary baseline, failing to account for natural physiological fluctuations over time. To overcome these limitations, we implemented a GAM framework that mathematically decomposes protein abundance into a shared baseline trend ($f_{baseline}$) representing natural fluctuations in untreated cells and condition-specific deviations (f_{diff}) capturing stress-induced responses. This dynamic modeling revealed that 1794 proteins (59.5% of the identified high-confidence proteome) exhibited significant temporal fluctuations even under control conditions (**Extended Fig. 4A**). Far from being static, the homeostatic proteome undergoes continuous remodeling—a finding that highlights the limitations of the conventional assumption of steady-state baselines and underscores the necessity of continuous background modeling to distinguish genuine stress responses from basal rhythms.

We first validated the continuous abundance trajectories reconstructed by the GAM framework, a model that incorporates both baseline homeostatic trends and condition-specific deviations, by analyzing canonical stress markers. The model's terminal abundance profiles accurately captured the expected repression of machinery involved in ribosome biogenesis (Rpl3), amino acid biosynthesis (Leu1), lipid metabolism (Fas2), and cell wall integrity (Kre6) under acetic acid stress (**Fig. 3A**), aligning with the global downregulation reported in previous transcriptomic endpoint studies[19]. Importantly, while these markers have been traditionally characterized as monotonic decreasing due to

the limitations of sparse sampling, our continuous profiling revealed that their progression is far from monotonic. The GAM trajectories unveiled a transient recovery phase: many repressed proteins displayed a distinct rebound during the mid-response period, suggesting an attempt to restore homeostasis before terminal collapse. Furthermore, our high-resolution kinetics provide a potential kinetic explanation for previously reported discrepancies regarding heat shock proteins (HSPs). While some studies suggest HSP upregulation[19] due to acidification-induced protein unfolding, others report downregulation[17]. Our temporal profiling of Hsp82 and Ssa4 revealed a complex, non-monotonic dynamic pattern: an initial transient induction was followed by a decline, a secondary failed recovery, and a final collapse (**Fig. 3B**). This transient induction, where initial activation is superseded by the global translational arrest[34], provides a kinetic explanation for the proteome-transcriptome decoupling frequently observed under lethal stress, and underscores why snapshot measurements yield opposing conclusions depending on sampling time.

To quantify the magnitude of protein responses under lethal stress relative to the control, we defined two complementary metrics derived from the GAM trajectories: Maximal Difference (MaxDiff) representing the peak amplitude of deviation and Root Mean Square Deviation (RMSD) as a stability filter to generate kinetic volcano Plots (**Fig. 3C**). Analogous to traditional differential analysis, our temporal volcano plots also identify proteins with significant shifts, such as the specific induction of cytochrome c isoform 1 (Cyc1), a classic hallmark of cell death. Given the extreme statistical power provided by 100 observation points per protein, traditional *p*-values exhibited a ceiling effect; however, this MaxDiff/RMSD framework effectively ranked the most biologically pertinent responders (**Fig. 3C**). To explore the functional biological programs driving these dynamic shifts, we performed Gene Set Enrichment Analysis (GSEA) based on the MaxDiff ranking (KEGG), which accurately recapitulated the functional logic observed in our clustering analysis: both lethal conditions exhibited a suppression of ribosome biogenesis, while acetic acid stress specifically upregulated oxidative phosphorylation (**Extended Fig 4B, C**). To further verify the reliability of using MaxDiff as a proxy for directional regulation (up- or down-regulation) in longitudinal data, we mapped ranked proteins against ESR gene sets[29,35]. By evaluating the density distribution of these benchmarks (**Extended Fig. 4D, E**), we found that ESR-induced and ESR-repressed genes autonomously segregated to the positive and negative poles of our ranking. This alignment validates that our kinetic model correctly captures the polarity of the global stress response and indicates that MaxDiff serves as an effective alternative to conventional log2 fold change metrics in high-frequency temporal analysis.

To translate individual protein responses into the temporal progression of biological processes, we performed time-resolved GSEA on the GAM-derived area under the curve (AUC) across 16 discretized time windows (window width = 6 min, see Methods) (**Fig. 3D, E**). The 6-min window was not arbitrarily selected, but was derived from frequency-domain analysis of the minute-scale proteomic trajectories, which identified this interval as a conservative temporal scale that preserves low-frequency biological regulatory signals while attenuating high-frequency stochastic noise. In this way, the original 100-min proteomic movie was compressed into 16 high-fidelity temporal states, enabling pathway activities to be interpreted at a signal-supported biological resolution rather than at every noisy minute-level fluctuation. This temporal integration, which enhances the detection of coordinated pathway responses by reducing the impact of transient noise, uncovered two fundamentally distinct trajectories of systemic failure.

In the acetic-acid-induced yN-RCD trajectory, time-resolved GSEA revealed a distinct sequence of molecular events (**Fig. 3D, Extended Fig. 4F**) initiating with an immediate surge in oxidative phosphorylation (3 min; e.g., Atp18, Cyc1, Rip1). Concurrently, we observed the upregulation of soluble N-ethylmaleimide-sensitive factor attachment protein receptors (SNARE) interactions (3 min; e.g., Sec22, Gos1, Vam7). Furthermore, we observed a concurrent suppression of propanoate metabolism (3-15 min; e.g., Acs1) along with glyoxylate and dicarboxylate metabolism (9-15 min; e.g., Mdh2, Ctt1). As the response progresses, the system reaches a turning point marked by the

upregulation of autophagy at 21 minutes (e.g., Atg13, Atg2). This mid-stage catabolic shift precedes the irreversible systemic decline. Consistent with this trajectory of systemic failure, key pathways governing cellular proliferation, specifically cell cycle (e.g., Cdc28) and ribosome biogenesis (e.g., Nop4), exhibited a continuous decline throughout the time course, confirming the irreversible cessation of growth and the progression toward terminal collapse.

In contrast, the H_2O_2-induced yA-RCD trajectory depicted a distinct temporal progression, unfolding across three distinct kinetic stages. The early phase (3-15 min) was dominated by a synchronized activation of DNA replication and multiple repair mechanisms (Base/Nucleotide excision/Mismatch repair) (**Fig. 3E, Extended Fig. 4G**). This was accompanied by a specific, transient burst in ribosome biogenesis (e.g., Pop6, Nob1, Utp9). However, simultaneously, mitophagy was significantly suppressed (3-9 min, e.g., Fis1, Bre5, Ckb1). The intermediate phase (15-27 min) featured a kinetic transition. Unlike the acetic acid induced response, SNARE interactions were initially suppressed (15 min, e.g., Vam3, Snc1). This coincided with the upregulation of steroid biosynthesis observed in our analysis (15-21 min) (**Extended Fig. 4G**). The trajectory culminated in systemic collapse (after 33 min). A kinetic inversion was observed, where DNA repair machinery shifted from activation to suppression. Concurrently, metabolic pathways exhibited a paradoxical resurgence in our GSEA map. However, inspection of individual protein traces revealed that this is not *de novo* activation, but rather a preferential preservation of core metabolic enzymes relative to the rapidly degrading proteome background. This distinct phase transition suggests the proteome has evolved into a state of criticality. Following this transition, the system enters an irreversible failure state.

Learning continuous proteome dynamics to infer upstream regulatory signals of cell death subroutines

While GAM provided rigorous statistical inference for individual proteins, it remains a univariate approach that treats proteins as independent entities. To address this limitation and capture the governing dynamics of the interconnected proteome system, we developed a deep learning model based on Conditional Latent Neural ODEs[36].

To ensure the model remained biologically interpretable, we translated the additive logic of our GAM statistical method into the neural architecture. Specifically, we modeled the evolution of the latent state $\mathbf{z}_c(t)$ in a low-dimensional latent space, where the time derivative $\frac{d\mathbf{z}_c(t)}{dt}$ was explicitly decomposed into two functional components: a shared field $\mathbf{F}_{\text{baseline}}(\mathbf{z}_c(t))$ capturing universal dynamics, and a condition-specific perturbation field $\mathbf{F}_{\text{diff}}(\mathbf{z}_c(t), \mathbf{e}_c)$ that uses treatment identity to model stress-specific dynamic deviations (**Fig. 4A**). This structurally constrained design allows the model to mathematically disentangle the stress response from the intrinsic homeostatic program over time, providing a clean computational foundation for our subsequent gradient-based discovery of upstream drivers.

To ensure that the learned latent space captured valid dynamics rather than overfitting to static snapshots, we adopted a reconstruction-based representation learning strategy. Instead of a standard forecasting task, the model was designed to encode the initial observation window (first 12 time points) into a latent initial state $\mathbf{z}_0$, and then generatively reconstruct the trajectory of the subsequent unobserved window (next 4 time points) solely by integrating the learned ODEs. In this framework, the comparison between the ODE-integrated trajectory and the held-out data serves as a structural constraint during training, whereby the model updates its parameters to minimize the reconstruction error on these future points. The model achieved high reconstruction fidelity on validation data, with coefficients of determination (R^2) exceeding 0.96 across all conditions (**Fig. 4B**). This performance indicates that the model has successfully approximated the underlying dynamics governing the system.

To rigorously validate that the model captures the underlying system dynamics, we performed a comparative PCA of the raw high-dimensional protein space versus the learned low-dimensional latent space (**Fig. 4C**). While the raw protein trajectories exhibited stochastic fluctuations and jagged transitions characteristic of measurement noise and biological variability, the latent manifolds revealed smooth, continuous evolution. Crucially, the latent trajectories for acetic acid and H_2O_2 originate from a common initial state and progressively bifurcate into topologically distinct paths. This contrast, together with the separation of the latent trajectories, suggests that the Neural ODE reduces high-frequency noise while encoding the high-dimensional proteomic state into a low-dimensional representation that preserves biologically relevant temporal structure.

Validation of the latent space geometry and unsupervised discovery of temporal regulatory signals via gradient analysis

To assess whether the learned latent representation captures meaningful biological transitions, we correlated individual protein trajectories with the first principal component (PC1) of the latent manifold, finding that the latent representation effectively mapped the proteome along an axis that we operationally define as a Growth-Death axis (**Fig. 5A**). To further validate this geometry, we benchmarked the PC1 rankings against canonical ESR gene sets[29,35] using density distribution analysis (**Fig. 5B**), which revealed separation, with ESR-repressed genes (growth associated) enriched toward the positive pole, while ESR-induced genes (stress-associated) were enriched toward the negative pole. This enhanced signal-to-noise ratio, significantly sharper than raw abundance metrics (**Extended Fig. 4D, E**), confirms that the Neural ODE effectively functions as a filter, extracting a robust biological manifold from high-frequency fluctuations. To characterize the biological features of these poles, we performed pathway enrichment analysis, finding that while the growth pole was defined by ribosome biogenesis, the death pole was enriched in endocytosis components (**Fig. 5C**). This indicates a shared terminal signature of systemic collapse across distinct lethal trajectories.

While abundance-based analysis (GAM) depicts the cumulative evolution of functional pathways, it primarily captures downstream physical accumulations. To identify proteins driving the trajectory of the system state, we performed a gradient-based saliency analysis leveraging our trained Neural ODE model. This analysis was performed on the same FFT-informed 16-window temporal grid used for abundance-based pathway analysis, allowing model-inferred regulatory influence to be directly compared with GAM-derived pathway dynamics at matched temporal states. Because the input data preserved absolute abundance scales without per-protein standardization, this saliency metric is not entirely independent of protein levels. Instead, it provides a complementary perspective. To compare these two metrics globally, we projected the proteome onto saliency-abundance scatter plots (**Extended Fig. 5A, B**), finding a general positive correlation ($r > 0.6$). This confirms that highly abundant proteins with large dynamic changes inherently exert significant influence on the system, validating our abundance-based findings. However, the gradient analysis uniquely highlights specific nodes whose temporal influence ranks disproportionately higher than their abundance shifts.

To uncover early regulatory drivers within the acetic-acid-induced yN-RCD trajectory, we performed time-resolved GSEA based on the gradient rankings, using the same 16 discretized temporal windows as in the GAM-based GSEA. This analysis identified an upstream pathway less apparent in the GAM analysis, as Basal transcription factors exhibited high saliency in the early phase (3 min) (**Fig. 5D**). To understand why this pathway was exclusively captured by the gradient approach, we examined individual protein contributions at this time point (**Extended Fig. 5A**). While specific factors like Taf3 and Spt15 exhibited both high abundance changes and high saliency, their individual abundance shifts were insufficient to support the statistical enrichment of the entire pathway in the GAM analysis. Conversely, the gradient analysis assigned higher rankings to other pathway members, such as Tfb2 and Toa2, relative to their abundance changes (shifting above the diagonal). This collective elevation in pathway-level saliency rankings enabled the detection of this early transcriptional

response. Consistent with these early saliency signals, our gradient-based GSEA recovered the downstream pathway-level dynamics identified by GAM, including the early enrichment of oxidative phosphorylation and SNARE interactions (3 min), the mid-phase enrichment of autophagy (from 21 to 27 min), and the progressive suppression of ribosome biogenesis (after 39 min).

Similarly, to assess the temporal progression in the H_2O_2-induced yA-RCD trajectory, we analyzed its condition-specific gradient profiles (**Fig. 5E**). Consistent with the abundance data, this analysis supported the early enrichment of DNA replication and repair pathways concurrent with ribosome biogenesis (from 3 to 15 min). To identify transitions in the intermediate phase, we focused on the 21 min window, where the gradient analysis highlighted mitophagy and peroxisome components. By examining the corresponding scatter plot, we found that although the global correlation remained positive, mitophagy (e.g., Cka2, Mdm10) and peroxisome proteins (e.g., Pex14, Idp2, Faa3) clustered in the high-saliency region above the diagonal relative to their abundance levels (**Extended Fig. 5B**). This positioning suggests that these pathways have greater saliency for model-predicted future proteome dynamics despite modest abundance changes. Consequently, gradient analysis provides a complementary approach to standard abundance profiling, highlighting events that may be underestimated by abundance metrics alone.

Systematic reconstruction of the temporal molecular patterns associated with yeast cell death

By integrating our high-resolution temporal abundance profiles, gradient-inferred candidate regulatory features, and established literature, we reconstructed a hypothetical systems view of yeast cell death under acute acetic acid and hydrogen peroxide stress (**Fig. 6**). Rather than a static inventory of stress-responsive pathways, this synthesis organizes isolated kinetic events into two distinct temporal patterns, revealing trade-offs that may contribute to the transition from adaptation to loss of viability.

In the acetic acid-induced yN-RCD trajectory, our integrated model suggests a temporal pattern of metabolic exhaustion (**Fig. 6A**). The proposed sequence begins with acetic acid entry via the Fps1 channel and its subsequent intracellular dissociation[37]. To limit further toxin flux, the cell triggers Hog1-mediated degradation of Fps1 while simultaneously activating basal transcription factors (captured by our 3 min gradient analysis) to initiate a rapid transcriptional response[38]. To counteract rapid cytosolic acidification, the cell mobilizes energy-intensive proton pumps including Pma1[39] and V-ATPase[40]. This physiological imperative provides a possible mechanistic explanation for our observed 3 min surge, in which the simultaneous upregulation of SNARE interactions may facilitate increased vesicular trafficking of these pumps to membrane sites, while oxidative phosphorylation increases to meet the elevated ATP demand. However, our temporal profiles suggest that this intensive response is associated with a substantial metabolic cost. The conversion of high levels of acetate to acetyl-CoA may deplete the cytosolic free CoA pool, potentially contributing to the concurrent suppression of alternative CoA-dependent pathways such as propanoate and glyoxylate metabolism observed in our abundance-based analysis. Sustained activation of mitochondria may promote ROS accumulation. The increased autophagy response we detected at 21 minutes thus may reflect a mid-stage catabolic shift rather than an early defense, attempting to support a bioenergetically compromised system before subsequent membrane integrity loss.

Conversely, the hydrogen peroxide-induced yA-RCD trajectory reveals a fundamentally different defensive logic characterized by genomic triage (**Fig. 6B**). Following entry via free diffusion or facilitated diffusion mediated by aquaporins[41], hydrogen peroxide is converted into highly toxic hydroxyl radicals through the Fenton reaction, directly inducing oxidative damage to the genome[7,42]. Our temporal map suggests that the cell's immediate response (from 3 to 15 min) involves preferential resource allocation, appearing to prioritize nuclear integrity through the synchronized activation of DNA repair pathways, potentially supported by a transient increase in ribosome biogenesis to synthesize *de novo* repair enzymes. However, this resource allocation, which appears to favor the

nucleus, may leave organelles vulnerable. This is consistent with the apparent early suppression of mitophagy observed in our data. Furthermore, unlike the acetic acid response, SNARE interactions are significantly suppressed, which may reflect reduced vesicular trafficking that could restrict membrane fluidity and limit the intracellular propagation of cytotoxic lipid peroxidation products[43,44]. In addition, our gradient analysis identified the later changes associated with this early resource allocation, with 21 minutes showing transient enrichment of clearance-related pathways (highlighted by the increased saliency of mitophagy and peroxisome components, alongside NADPH-producing metabolic changes). The insufficiency of this delayed organelle response may promote a ROS-induced ROS-release positive feedback loop[43,45], potentially contributing to the kinetic inversion and loss of system stability observed after 33 minutes.

Anchoring the molecular trajectories to the loss of clonogenic potential

To assess the physiological relevance of these computationally derived temporal patterns, we performed time resolved clonogenic assays on the acetic acid trajectory to determine the temporal boundary associated with loss of reproductive capacity (**Fig. 7A, B**). By exposing yeast cultures to stress for specific durations followed by immediate washout and plating, we assessed their residual capacity to resume cellular division.

The results showed a steep decline in reproductive viability within the initial 15 minutes, plateauing at a near-zero baseline from 21 minutes onwards ($P > 0.05$). This indicates that by 21 minutes, the population had effectively lost its reproductive potential. Consistently, our high-frequency proteomics, which captures the instantaneous molecular profile via immediate quenching, shows that the autophagy activation pulse reaches its highest ranking at this 21-minute mark. While autophagy canonically functions as a pro-survival mechanism to sustain cellular energy and clear damage, its maximal activation coinciding with the loss of reproductive viability supports a context-dependent role in this lethal trajectory. This massive catabolic mobilization represents a terminal scavenging response that maintains immediate metabolic persistence and delays physical lysis, but is ultimately insufficient to salvage the cell's capacity to divide. Therefore, in the acetic-acid-induced yN-RCD trajectory, the 21-minute mark represents a definitive Point of No Return, characterized by the convergence of reproductive death and the activation of late catabolic programs.

Discussion

A mechanistic understanding of regulated cell death requires moving beyond the cataloging of static molecular markers to resolve how molecular responses unfold during the execution process. Although endpoint measurements have defined many hallmarks of cell death[13], our results show that minute-scale temporal proteomics can reveal biological features that are difficult to capture by traditional static analyses. In addition, we provide an integrated methodological workflow spanning high-frequency sampling, latent dynamic modeling, and biological interpretation, which may serve as a reference for future studies of highly dynamic cellular processes.

A central biological insight from our high-resolution temporal map is that terminal cellular collapse can be shaped by the costs of the cell’s own adaptive defenses. Rather than simply reflecting passive damage accumulation, the two lethal trajectories involve distinct physiological trade-offs. In the acetic-acid-induced yN-RCD trajectory, an energy intensive response to acidification is associated with metabolic exhaustion. In the hydrogen-peroxide-induced yA-RCD trajectory, genomic triage appears to prioritize nuclear repair while leaving organelle quality control vulnerable to oxidative damage. This continuous view suggests that early defense mechanisms, although initially adaptive, can impose resource demands and vulnerabilities that contribute to later system failure.

Our high-temporal-resolution profiling also helps reconcile conflicting conclusions from traditional static studies, such as discrepancies regarding heat shock protein regulation[17,19]. By revealing non-

monotonic trajectories with transient recoveries, kinetic inversions, and brief activation pulses, our data show how sparse sampling can be sensitive to the selected time point. This highlights the importance of continuous observation for distinguishing sustained stress responses from transient homeostatic fluctuations.

Importantly, aligning these high-frequency molecular trajectories with time-resolved survival assays allowed us to define a biological Point of No Return in the acetic-acid-induced trajectory. Reproductive viability declined to a near zero baseline from 21 minutes onward, while autophagy reached its strongest activation at the same time point. Although autophagy canonically functions as a pro-survival mechanism to sustain cellular energy and clear damage, its activation coinciding with the loss of reproductive viability supports a context-dependent role in this lethal condition. Specifically, late autophagy may represent a terminal scavenging response that maintains immediate metabolic persistence but is insufficient to restore the cell's capacity to divide. Thus, the 21 minute mark represents a definitive Point of No Return in this trajectory, characterized by the convergence of reproductive death and late catabolic activation.

Methodologically, our Neural ODE-based gradient analysis provides a complementary way to interpret longitudinal omics data, where regulatory signals may precede or be masked by protein abundance changes. By estimating dynamic saliency within a learned latent space, this approach helped prioritize candidate temporal features whose influence on model-predicted future states was greater than expected from abundance changes alone. This was useful for identifying early basal transcription factor signals in the acetic-acid-induced yN-RCD trajectory and delayed mitophagy and peroxisome related signals in the hydrogen-peroxide-induced yA-RCD trajectory. Therefore, rather than replacing abundance based analysis, gradient based modeling can complement it by highlighting candidate regulatory events that may be underestimated by endpoint or abundance centered approaches.

Future integration of post-translational modifications[46], metabolite dynamics, and single-cell measurements[47] will be important for refining these temporal models and testing the proposed mechanisms. Nevertheless, our current findings support the value of high-frequency temporal profiling for studying dynamic biological processes. Together, the results show that the biology of cell death is encoded not only in which proteins change, but also in when and how those changes occur. This study therefore provides both biological insight into yeast regulated cell death and a practical analytical workflow for measuring and interpreting rapid cellular state transitions.

Materials and methods

Yeast culture and high-frequency time-series collection

S. cerevisiae strain BY4741 was cultured in YPD medium at 30°C with orbital shaking (200 rpm). To establish a reproducible system for high-frequency sampling, cells were grown to mid-log phase ($OD_{600} \approx 1.0$). The culture was then split into three independent 50 mL reaction systems maintained in a thermostatic shaker within a laminar flow hood to allow simultaneous sampling. Stress treatments were initiated by adding pre-calculated stock solutions to achieve the following final conditions: (1) Control: water vehicle; (2) Acetic Acid: 400 mM; and (3) Hydrogen Peroxide (H_2O_2): 5 mM.

To generate the high-frequency samples, aliquots (400 µL) were withdrawn from each biological reaction system at 1-minute intervals for a duration of 100 minutes. Cellular activity was instantly quenched by mixing the sample with trichloroacetic acid (TCA) to a final concentration of 10% (v/v), followed by incubation on ice[26]. Cells were harvested by centrifugation (3,500 × g, 5 min, 4°C), and the pellets were washed twice with ice-cold acetone to remove residual TCA and contaminants. The dried pellets were stored at -80°C until further processing.

Proteomics data acquisition

Protein extraction and digestion were performed using Pressure Cycling Technology (PCT), as previously described[48,49], with study-specific modifications. Briefly, cell pellets were resuspended in 30 µL lysis buffer (6 M Urea, 2 M Thiourea) supplemented with 5 µL TCEP and 2.5 µL IAA. Lysis was carried out in a Barocycler (Pressure BioSciences) with PCT-MicroTubes using 90 cycles of alternating pressure (45 kpsi for 30 s, ambient pressure for 10 s) at 30°C. Following lysis, samples were diluted with 100 mM ammonium bicarbonate to reduce urea concentration < 1 M. Digestion was performed in a single step by adding Lys-C at a 1:80 (enzyme:protein) ratio and Trypsin at a 1:20 ratio. The digestion was accelerated by PCT using 120 cycles (20 kpsi for 50 s, ambient pressure for 10 s) at 30°C. The reaction was terminated with trifluoroacetic acid (TFA, final 1%), and peptides were desalted using C18 columns, dried under vacuum, and reconstituted in 0.1% formic acid to a concentration of 0.25 µg/µL for LC-MS analysis.

To ensure deep proteome coverage, a yeast spectral library was constructed using five *S. cerevisiae* strains (BY4741, BY4742, S288C, SEY6210, W303). Peptides from a pooled sample were fractionated into 120 fractions using high-pH reversed-phase chromatography, which were consolidated into 60 fractions for LC-MS/MS analysis. Data were acquired in Data-Dependent Acquisition (DDA) mode on a Q Exactive HF mass spectrometer (Thermo Fisher Scientific). The library was generated using Spectronaut (v14.6.201001.47784)[50].

Peptides from the experimental samples were analyzed on a Q Exactive HF hybrid Quadrupole-Orbitrap mass spectrometer coupled to a Dionex UltiMate 3000 RSLCnano system (Thermo Fisher Scientific). For Data-Independent Acquisition (DIA), the MS1 scan range was set to 390-1010 m/z at a resolution of 60,000, with an AGC target of 3e6 and a maximum ion injection time of 80 ms. MS2 scans were acquired at a resolution of 30,000 with an AGC target of 1e6 and an auto mode of maximum ion injection time. The normalized collision energy (NCE) was set to 28. The raw files were analyzed using DIA-NN (2.0 Academia)[27] against our yeast spectral library. The spectral library for yeast contains 218,818 proteotypic peptides and 5238 protein groups. In the DIA-NN setting, RT profiling was performed and other parameters were set to default. Quantitative data for precursor and proteins were both controlled below 1% FDR.

Time-series colony-forming unit assay

S. cerevisiae cells from pre-cultures were diluted to a final OD_{600} of 1.0 and subjected to stress treatment with a final concentration of 400 mM acetic acid. Aliquots were harvested at specified time intervals (e.g., 3, 9, and 15 min) post-treatment. To immediately halt the stress exposure, the samples were centrifuged (500 × g, 3 min) and the acetic acid-containing supernatant was discarded. The resulting cell pellets were washed twice by resuspension in PBS followed by centrifugation (500 × g, 3 min) to thoroughly eliminate residual acetic acid. Subsequently, equal volumes of the washed cell suspensions were serially diluted and spread onto solid YPD agar plates. The plates were incubated at 30°C for 48 hours, after which they were photographed and the viable colonies were enumerated to assess cell survival.

Preprocessing of the protein matrix and quality control

The protein group matrix of DIA-NN results was used to do the downstream data analysis. To stabilize the variance across the wide dynamic range of protein abundance, intensity values were log2-transformed. Subsequently, quantile normalization was applied using the preprocessCore R package[51] to align the intensity distributions across all samples, ensuring comparability while preserving biological variability. Given the large-scale longitudinal design (22 PCT batches), systematic technical variations arising from instrument performance and sample preparation were observed. To preserve biological temporal trends that might be distorted by commonly used batch correction algorithms like ComBat[52,53] and Limma[54], we adopted a reference-based ratio method [28]. Our experimental design incorporated pooled peptide mixtures and biological QC samples (untreated yeast prepared alongside

time-series samples) to monitor instrument and sample preparation variability, respectively. To address the potential non-linear superposition of these technical artifacts, we implemented a two-step correction strategy: first, correcting for instrument drift using the pooled reference within each batch; second, removing preparation-specific bias using the QC reference. To ensure the robustness of longitudinal profiling, stringent quality control criteria were applied to the corrected protein abundance matrix. First, proteins quantified in fewer than 60% of samples (missing rate > 40%) were excluded to minimize noise arising from stochastic detection of low-abundance features. Second, four samples exhibiting instrumental anomalies during MS acquisition were removed from the dataset. To facilitate downstream time-series modeling algorithms that require complete data matrices (e.g., maSigPro, Neural ODE), remaining missing values were imputed using a K-means-based strategy[55]. Specifically, proteins with complete observations across all time points were first clustered into k=5 representative temporal patterns using the K-means algorithm (R stats package, nstart = 25). For proteins containing missing values, the Euclidean distance to each cluster centroid was calculated based solely on the available observed time points. Missing values were then substituted with the corresponding intensities from the nearest cluster centroid. This approach imputed a total of 68,100 missing values, representing 7.56% of the total dataset (900,887 data points), thereby preserving the underlying temporal structures while enabling comprehensive analysis. The resulting high-quality data matrix comprised 3,013 protein groups quantified across 299 time-series samples (Control: n=99; H_2O_2: n=100; Acetic Acid: n=100), which served as the standardized input for all subsequent statistical modeling and machine learning analyses (**Extended Fig. 1B**).

Frequency-domain analysis and signal denoising

While the reference-based ratio method effectively removed systematic batch effects, high-frequency sampling at 1-minute intervals inherently captures stochastic noise and instrumental spikes that can obscure biological trends (**Extended Fig. 2A**). To rigorously distinguish biologically relevant temporal dynamics from high-frequency noise without relying on arbitrary smoothing parameters, we performed a spectral analysis. This analysis was used to define the temporal scale at which biological signals could be robustly interpreted, rather than to simply reduce the number of time points.

First, expression profiles for each protein were detrended by mean subtraction. This detrending step removed protein-specific offsets and allowed the subsequent frequency-domain analysis to focus on temporal fluctuation patterns rather than baseline abundance differences. The Power Spectral Density (PSD) was subsequently computed using the Fast Fourier Transform (FFT) algorithm to quantify the distribution of signal variance across frequency components. A global PSD profile for each treatment condition was generated by averaging PSD values across all proteins. The averaged PSD profiles showed that most signal power was concentrated in the low-frequency range, whereas higher-frequency components approached a noise-dominated regime, consistent with the presence of minute-scale stochastic fluctuations and occasional instrumental spikes. To identify the cutoff frequency ($f_{\mathrm{cut},g}$) separating the dominant biological signal from the noise floor, we applied the Elbow Method to the log-log plots of mean PSD versus frequency. The elbow point was geometrically defined as the coordinate that maximizes the perpendicular distance to the line connecting the spectral extremes (**Extended Fig. 2B**). This data-driven criterion avoids manually selecting a smoothing parameter and provides an objective transition point between structured temporal variation and high-frequency noise.

To ensure a conservative filtering strategy that preserves the fastest biological responses, we selected the maximum cutoff frequency among all treatment groups:

$$f_{\max} = \max_{g} f_{\mathrm{cut},g}.$$

Using the maximum rather than the average cutoff frequency minimizes the risk of oversmoothing condition-specific rapid responses, because the final window is determined by the fastest resolvable

biological dynamics observed across the dataset. The optimal temporal window size (w) was then derived according to the Nyquist-Shannon sampling theorem[56]:

$$w \approx \frac{1}{2f_{\max}}.$$

This yielded a calculated window of

$$w = 6 \text{ min}.$$

Thus, the 6-min interval represents an FFT-informed estimate of the shortest temporal scale at which proteome-wide biological dynamics can be interpreted with improved signal-to-noise support. Based on this theoretically derived window, two distinct denoised datasets were generated to suit specific downstream analytical requirements:

1. Smoothed dataset (Moving Average): A centered rolling average with w=6 was applied to the full time-series. This dataset retained the original temporal density (100 time points) to maximize statistical power for trend-fitting algorithms, including maSigPro, WGCNA, and GAM analysis (**Extended Fig. 2C**). Therefore, the smoothed dataset preserved minute-scale temporal continuity while reducing local stochastic fluctuations, making it suitable for fitting continuous abundance trajectories.

2. Downsampled dataset (Median Binning): The time series was discretized into 16 bins (grouping every 6 minutes), with the median intensity representing each interval. This dataset was utilized for Neural ODE functional evolution analysis and interpretation, aligning the data granularity with the biological time scale of protein-level regulatory events (~6 min) to ensure robust feature extraction (**Extended Fig. 2D**). The median was used to reduce the influence of isolated spikes within each window. This 16-window representation served as a common temporal coordinate system for time-resolved GSEA, Neural ODE training, and gradient-based saliency analysis, ensuring that abundance-derived pathway activities and model-inferred regulatory drivers were compared at matched, signal-supported temporal states.

Unsupervised clustering of temporal profiles

To systematically categorize proteome-wide temporal patterns, we applied the maSigPro[57] (microarray Significant Profiles) algorithm (v1.82.0) to the smoothed dataset. Adjacent groups of three consecutive time points were treated as biological replicates of their median time interval (Bin size = 3). This approach not only satisfied the algorithmic requirement for replicates but also further stabilized local trends against high-frequency noise. A polynomial regression model of degree 4 (degree = 4) was fitted to each protein profile. Significant proteins were identified using a false discovery rate (FDR) control of 0.05 (p.vector, Q = 0.05). Subsequently, a stepwise regression (T.fit, step.method = "backward") was performed. To prioritize proteins with biologically substantial dynamic changes, we applied a stringent goodness-of-fit filter (R^2>0.75). The resulting significant proteins were grouped into 6 distinct clusters based on their temporal profiles using hierarchical clustering (see.genes, k = 6).

To identify functional protein modules based on co-expression patterns rather than just trend similarity, we performed WGCNA (v1.73) [58]. The smoothed protein expression matrix was used as input. First, a soft-thresholding power of β=30 was selected. An adjacency matrix was calculated using biweight midcorrelation (bicor) to minimize the effect of outliers, and transformed into a topological overlap matrix (TOM). Protein modules were identified using the blockwiseModules function with a minimum module size of 5 and a merge cut height of 0.2. The Module Eigengene (ME) was calculated for each module and correlated with external traits (Treatment, Time). Hub proteins were defined as those with high module membership and exported for network visualization in Cytoscape.

Functional enrichment and benchmark validation

Biological functions were annotated using clusterProfiler (v4.18.3)[59] with the *S. cerevisiae* genome database (org.Sc.sgd.db). *P*-values were adjusted using the Benjamini-Hochberg procedure (FDR < 0.05). To rigorously verify the biological relevance of our findings, we benchmarked our clusters against the canonical ESR gene sets[29,35]. Crucially, to prevent statistical inflation, the background universe for the Fisher's exact test was strictly defined as the intersection between the canonical ESR gene list and the 3013 proteins quantified in our study. The significance of the overlap between each proteomic cluster/module and the specific ESR-Repressed or ESR-Induced sets was then evaluated based on this defined background.

Generalized additive models

To rigorously disentangle condition-specific protein dynamics from baseline temporal trends, we implemented a GAM framework using the mgcv R package. For each protein p, the log2-transformed abundance $Y_{p,c,i}$ at time point t_i under condition c was modeled as:

$$Y_{p,c,i} = \beta_{0,p} + \beta_{c,p} + f_{p,\text{baseline}}(t_i) + f_{p,\text{diff},c}(t_i) + \varepsilon_{p,c,i}.$$

Here, p indexes the protein, c indexes the experimental condition, and i indexes the sampled time point. The condition set was defined as

$$\mathcal{C} = \{\text{Control}, \text{H}_2\text{O}_2, \text{Acetic Acid}\}.$$

The term $\beta_{0,p}$ represents the protein-specific global intercept, and $\beta_{c,p}$ captures the condition-specific mean abundance offset relative to the control condition. The smooth function $f_{p,\text{baseline}}(t)$ represents the shared temporal trend for protein p, corresponding to the baseline smooth, whereas $f_{p,\text{diff},c}(t)$ captures the condition-specific deviation from the baseline trajectory, corresponding to the difference smooth. In the reference parameterization, the control condition was treated as the baseline condition. Thin-plate regression splines were used as basis functions with basis dimension $k = 7$, balancing curve smoothness and flexibility. Models were fitted using restricted maximum likelihood estimation.

We performed two distinct statistical tests to characterize protein dynamics. First, to identify proteins that changed over time even under homeostatic conditions, we tested the baseline trend null hypothesis

$$H_{0,p}^{\text{baseline}}: f_{p,\text{baseline}}(t) = 0 \quad \text{for all } t.$$

Second, to identify stress-responsive proteins whose trajectories significantly diverged from the control trajectory, we tested the condition-specific difference null hypothesis

$$H_{0,p,c}^{\text{diff}}: f_{p,\text{diff},c}(t) = 0 \quad \text{for all } t.$$

P-values were adjusted for multiple hypothesis testing using the Benjamini-Hochberg procedure, with FDR < 0.05 considered significant.

Definition of MaxDiff and RMSD

To quantify the magnitude and stability of the stress response, we derived two metrics from the fitted continuous trajectories. Let $\hat{Y}_{p,c}(t)$ denote the fitted abundance trajectory of protein p under condition c, and let $\hat{Y}_{p,\text{ctrl}}(t)$ denote the corresponding fitted trajectory under the control condition. The fitted difference trajectory was defined as

$$\hat{\Delta}_{p,c}(t) = \hat{Y}_{p,c}(t) - \hat{Y}_{p,\text{ctrl}}(t).$$

The Maximal Difference, MaxDiff, serves as a dynamic proxy for fold change. It was defined as the signed difference at the time point where the absolute deviation between treatment and control trajectories is maximized. Specifically,

$$t^*_{p,c} = \arg\max_{t\in[0,T]} \left|\hat{\Delta}_{p,c}(t)\right|,$$

and

$$\mathrm{MaxDiff}_{p,c} = \hat{\Delta}_{p,c}\left(t^*_{p,c}\right).$$

Equivalently,

$$\mathrm{MaxDiff}_{p,c} = \hat{Y}_{p,c}\left(t^*_{p,c}\right) - \hat{Y}_{p,\mathrm{ctrl}}\left(t^*_{p,c}\right).$$

To distinguish sustained biological responses from transient fluctuations, we calculated the Root Mean Square Deviation (RMSD), representing the average magnitude of divergence across the entire time course T:

$$\mathrm{RMSD}_{p,c} = \sqrt{\frac{1}{T}\int_0^T \left[\hat{Y}_{p,c}(t) - \hat{Y}_{p,\mathrm{ctrl}}(t)\right]^2 dt}.$$

Proteins were considered biologically significant if they passed the FDR threshold of 0.05 and ranked within the top 50% of RMSD values.

GAM-based time-resolved functional enrichment analysis

To decode the temporal evolution of pathway activities, we performed time-resolved GSEA. The continuous 100-min time course was discretized into 16 bins using the FFT-informed window size $w = 6$ min. For each comparison c_1 versus c_0, each bin B_b contained six consecutive grid points from the dense GAM prediction grid. We computed an unscaled binned AUC score from the fitted contrast between the two condition-specific GAM trajectories:

$$\mathrm{AUC}_{p,c_1,c_0,b} = \sum_{t_\ell \in B_b} \left[\hat{Y}_{p,c_1}(t_\ell) - \hat{Y}_{p,c_0}(t_\ell)\right].$$

Here, c_1 and c_0 denote the two compared conditions, and B_b denotes the set of six grid points in bin b. This binned sum is proportional to a Riemann approximation of the AUC of the fitted contrast trajectory. Because the grid spacing is constant across proteins within each bin, omitting the constant Δt scaling factor does not affect protein ranking for GSEA. The three contrasts analyzed were acetic acid versus control, hydrogen peroxide versus control, and acetic acid versus hydrogen peroxide. Proteins were ranked by $\mathrm{AUC}_{p,c_1,c_0,b}$ within each time window, and GSEA was performed using clusterProfiler against the KEGG database to identify pathways that were systematically activated, $\mathrm{AUC} > 0$, or suppressed, $\mathrm{AUC} < 0$, at specific temporal stages.

Conditional latent neural ordinary differential equations

To capture the continuous system dynamics and uncover potential drivers from high-dimensional proteomic data, we developed a conditional latent neural ODE model. The framework consists of three components: an encoder, a conditional ODE solver, and a decoder.

Encoder

We employed a Gated Recurrent Unit (GRU) [60] to map the observed time-series data into a distribution of initial latent states. Let $\mathbf{x}_c(t_m) \in \mathbb{R}^{D_{\mathrm{input}}}$ denote the protein abundance vector for condition c at time bin m, where D_{input} is the number of input protein features. The observed sequence was denoted as

$$\mathbf{X}_{\mathrm{obs}} = \left[\mathbf{x}_c(t_1), \mathbf{x}_c(t_2), \ldots, \mathbf{x}_c\left(t_{N_{\mathrm{obs}}}\right)\right] \in \mathbb{R}^{N_{\mathrm{obs}}\times D_{\mathrm{input}}}.$$

The encoder mapped $\mathbf{X}_{\mathrm{obs}}$ into a distribution over the initial latent state $\mathbf{z}_{t_0} \in \mathbb{R}^{D_{\mathrm{latent}}}$, where $D_{\mathrm{latent}} = 128$. The approximate posterior distribution was defined as

$$q_\phi\left(\mathbf{z}_{t_0} \mid \mathbf{X}_{\mathrm{obs}}\right) = \mathcal{N}\left(\boldsymbol{\mu}_\phi, \mathrm{diag}\left(\boldsymbol{\sigma}^2_\phi\right)\right).$$

The latent initial state was sampled using the reparameterization trick:

$$\mathbf{z}_{t_0} = \boldsymbol{\mu}_\phi + \boldsymbol{\sigma}_\phi \odot \boldsymbol{\epsilon}, \boldsymbol{\epsilon} \sim \mathcal{N}(\mathbf{0}, \mathbf{I}),$$

where $\odot$ denotes element-wise multiplication.

Conditional ODE Function

The core dynamics were governed by a learnable vector field that defines the time derivative of the latent state. To explicitly model stress responses, we decomposed the latent vector field into a shared baseline component and a condition-specific component:

$$\frac{d\mathbf{z}_c(t)}{dt} = \mathbf{F}_{\text{baseline}}\big(\mathbf{z}_c(t)\big) + \mathbf{F}_{\text{diff}}(\mathbf{z}_c(t), \mathbf{e}_c).$$

Here, $\mathbf{z}_c(t) \in \mathbb{R}^{D_{\text{latent}}}$ is the latent state under condition c at continuous time t, and $\mathbf{e}_c$ is a condition code vector used to encode treatment identity. The function $\mathbf{F}_{\text{baseline}}$ captures shared temporal dynamics, whereas $\mathbf{F}_{\text{diff}}$ captures condition-specific perturbation dynamics. Both vector fields map latent states to latent-state derivatives in $\mathbb{R}^{D_{\text{latent}}}$.

Both $\mathbf{F}_{\text{baseline}}$ and $\mathbf{F}_{\text{diff}}$ were parameterized by neural networks with one hidden layer of dimension $D_{\text{hidden}} = 256$ and Tanh activation functions. The continuous latent trajectory $\mathbf{z}_c(t)$ was computed by integrating this autonomous ODE from t_0 to t_N using the dopri5 solver, corresponding to the Dormand-Prince method, via the torchdiffeq library.

Decoder

A multilayer perceptron (MLP) decoder mapped the latent state back to the high-dimensional protein abundance space, followed by a condition-specific static shift:

$$\hat{\mathbf{x}}_c(t) = g_\theta\big(\mathbf{z}_c(t)\big) + \boldsymbol{\delta}_c.$$

Here, $\hat{\mathbf{x}}_c(t) \in \mathbb{R}^{D_{\text{input}}}$ is the reconstructed protein abundance vector at time t, g_θ denotes the decoder parameterized by θ, and $\boldsymbol{\delta}_c \in \mathbb{R}^{D_{\text{input}}}$ is a condition-specific static shift vector. The static shift vector for the control condition was constrained to zero.

Training strategy and loss function

To ensure that the model learned causal dynamics rather than simple interpolation, we implemented a forecasting training strategy. The model was trained to encode the first N_{obs} time points, corresponding to the observation window, and predict the subsequent N_{pred} time points, corresponding to the prediction window. To robustly validate model performance, we conducted a systematic series of experiments varying N_{obs} from 12 down to 1 using the downsampled dataset of 16 time bins.

The objective function was a weighted sum of the reconstruction loss and the Kullback-Leibler divergence:

$$\mathcal{L} = \text{MSE}\big(\mathbf{X}_{\text{true}}, \widehat{\mathbf{X}}_{\text{pred}}\big) + \lambda_{\text{KL}} D_{\text{KL}}\big[\, q_\phi\big(\mathbf{z}_{t_0} \mid \mathbf{X}_{\text{obs}}\big) \parallel \mathcal{N}(\mathbf{0}, \mathbf{I}) \,\big].$$

Here, $\mathbf{X}_{\text{true}}$ denotes the held-out future protein abundance matrix, $\widehat{\mathbf{X}}_{\text{pred}}$ denotes the model-predicted future abundance matrix, and λ_{KL} is the KL-divergence weight. The value of λ_{KL} was annealed from 0 to 0.01 during training. Optimization was performed using the Adam optimizer with a learning rate of 5×10^{-4} and a patience-based early stopping mechanism with patience set to 600 epochs.

Interpretation of the latent space

To decode the biological semantics of the learned representation, we extracted the continuous latent trajectories $\mathbf{z}_c(t)$ for all conditions across 16 time bins. A global latent state matrix was constructed by stacking these latent state vectors:

$$\mathbf{Z} = [\mathbf{z}_c(t_m)]_{c \in \mathcal{C},\, m=1,\ldots,16} \in \mathbb{R}^{(3\times 16)\times D_{\text{latent}}}.$$

We performed principal component analysis (PCA) on $\mathbf{Z}$ to identify the dominant axes of variation. To biologically annotate the principal components, we correlated the PC scores of the latent states with protein abundance profiles. Specifically, let $s_{k,c,m}$ denote the score of latent state $\mathbf{z}_c(t_m)$ on PC k. For each protein j, we defined its abundance vector across all condition-time states as

$$\mathbf{x}_j = \left(x_{j,c,m}\right)_{c,m},$$

and the corresponding PC score vector as

$$\mathbf{s}_k = \left(s_{k,c,m}\right)_{c,m}.$$

The association between protein j and PC k was then quantified using the Pearson correlation coefficient

$$r_{j,k} = \mathrm{cor}\left(\mathbf{x}_j, \mathbf{s}_k\right).$$

Proteins were ranked by $r_{j,\mathrm{PC1}}$, and GSEA was performed to identify pathways associated with the positive, Growth, and negative, Death, poles of the PC1 axis.

Gradient-based identification of temporal drivers

To identify key molecular drivers of the system trajectory, we employed reconstruction saliency analysis, which computes the gradient of the reconstruction loss with respect to the input features. Let $\mathcal{L}_{\mathrm{recon}}$ denote the reconstruction loss. The saliency vector for condition c at time t_m was defined as

$$\mathbf{S}_c(t_m) = \left|\nabla_{\mathbf{x}_c(t_m)}\mathcal{L}_{\mathrm{recon}}\right|,$$

where $\mathbf{S}_c(t_m) \in \mathbb{R}^{D_{\mathrm{input}}}$, and the absolute value is taken element-wise. For protein p, the protein-level saliency score was

$$S_{p,c}(t_m) = \left|\frac{\partial \mathcal{L}_{\mathrm{recon}}}{\partial x_{p,c}(t_m)}\right|.$$

This quantity measures the influence of protein p's abundance at time t_m on the model's ability to reconstruct or predict the system trajectory. A high absolute gradient value indicates that the protein is a critical determinant of system dynamics at that specific moment.

To create a directional ranking for GSEA, we calculated a signed saliency score. This score integrates the magnitude of influence from the gradient analysis with the direction of change from the GAM analysis. For each stress condition c, the saliency difference relative to the control condition was defined as

$$\Delta S_{p,c}(t_m) = S_{p,c}(t_m) - S_{p,\mathrm{ctrl}}(t_m).$$

The signed saliency score was then computed as

$$\mathrm{Score}_{p,c}(t_m) = \left|\Delta S_{p,c}(t_m)\right| \mathrm{sign}\left[\hat{f}_{p,\mathrm{diff},c}(t_m)\right].$$

Here, $\left|\Delta S_{p,c}(t_m)\right|$ represents the magnitude of the saliency difference between the stress and control conditions, whereas $\mathrm{sign}\left[\hat{f}_{p,\mathrm{diff},c}(t_m)\right]$ provides the direction of regulation inferred from the GAM-derived difference smooth. This formulation ensures that the ranking metric reflects both model-inferred importance and empirically observed direction of regulation. Proteins were then ranked by $\mathrm{Score}_{p,c}(t_m)$ at each time point, and time-resolved GSEA was performed to identify pathways that transiently drive the divergence between stress and control trajectories.

References

1. de Nadal, E., Ammerer, G., and Posas, F. (2011). Controlling gene expression in response to stress. Nat Rev Genet *12*, 833-845. https://doi.org/10.1038/nrg3055.
2. Wu, Y., Wu, J., Deng, M., and Lin, Y. (2021). Yeast cell fate control by temporal redundancy modulation of transcription factor paralogs. Nat Commun *12*, 3145. https://doi.org/10.1038/s41467-021-23425-0.
3. Galluzzi, L., Vitale, I., Aaronson, S.A., Abrams, J.M., Adam, D., Agostinis, P., Alnemri, E.S., Altucci, L., Amelio, I., Andrews, D.W., et al. (2018). Molecular mechanisms of cell death: recommendations of the Nomenclature Committee on Cell Death 2018. Cell Death Differ *25*, 486-541. https://doi.org/10.1038/s41418-017-0012-4.
4. Carmona-Gutierrez, D., Bauer, M.A., Zimmermann, A., Aguilera, A., Austriaco, N., Ayscough, K., Balzan, R., Bar-Nun, S., Barrientos, A., Belenky, P., et al. (2018). Guidelines and recommendations on yeast cell death nomenclature. Microb Cell *5*, 4-31. https://doi.org/10.15698/mic2018.01.607.
5. Madeo, F., Frohlich, E., Ligr, M., Grey, M., Sigrist, S.J., Wolf, D.H., and Frohlich, K.U. (1999). Oxygen stress: a regulator of apoptosis in yeast. J Cell Biol *145*, 757-767. https://doi.org/10.1083/jcb.145.4.757.
6. Almeida, B., Buttner, S., Ohlmeier, S., Silva, A., Mesquita, A., Sampaio-Marques, B., Osorio, N.S., Kollau, A., Mayer, B., Leao, C., et al. (2007). NO-mediated apoptosis in yeast. J Cell Sci *120*, 3279-3288. https://doi.org/10.1242/jcs.010926.
7. Konat, G.W. (2003). H2O2-induced higher order chromatin degradation: a novel mechanism of oxidative genotoxicity. J Biosci *28*, 57-60. https://doi.org/10.1007/BF02970132.
8. Ribeiro, G.F., Corte-Real, M., and Johansson, B. (2006). Characterization of DNA damage in yeast apoptosis induced by hydrogen peroxide, acetic acid, and hyperosmotic shock. Mol Biol Cell *17*, 4584-4591. https://doi.org/10.1091/mbc.e06-05-0475.
9. Martins, V.M., Fernandes, T.R., Lopes, D., Afonso, C.B., Domingues, M.R.M., Corte-Real, M., and Sousa, M.J. (2019). Contacts in Death: The Role of the ER-Mitochondria Axis in Acetic Acid-Induced Apoptosis in Yeast. J Mol Biol *431*, 273-288. https://doi.org/10.1016/j.jmb.2018.11.002.
10. Sokolov, S., Knorre, D., Smirnova, E., Markova, O., Pozniakovsky, A., Skulachev, V., and Severin, F. (2006). Ysp2 mediates death of yeast induced by amiodarone or intracellular acidification. Biochim Biophys Acta *1757*, 1366-1370. https://doi.org/10.1016/j.bbabio.2006.07.005.
11. Ludovico, P., Rodrigues, F., Almeida, A., Silva, M.T., Barrientos, A., and Corte-Real, M. (2002). Cytochrome c release and mitochondria involvement in programmed cell death induced by acetic acid in Saccharomyces cerevisiae. Mol Biol Cell *13*, 2598-2606. https://doi.org/10.1091/mbc.e01-12-0161.
12. Pereira, C., Camougrand, N., Manon, S., Sousa, M.J., and Corte-Real, M. (2007). ADP/ATP carrier is required for mitochondrial outer membrane permeabilization and cytochrome c release in yeast apoptosis. Mol Microbiol *66*, 571-582. https://doi.org/10.1111/j.1365-2958.2007.05926.x.
13. Chaves, S.R., Rego, A., Santos-Pereira, C., Sousa, M.J., and Corte-Real, M. (2025). Current and novel approaches in yeast cell death research. Cell Death Differ *32*, 207-218. https://doi.org/10.1038/s41418-024-01298-2.
14. Silva, A., Sampaio-Marques, B., Fernandes, A., Carreto, L., Rodrigues, F., Holcik, M., Santos, M.A., and Ludovico, P. (2013). Involvement of yeast HSP90 isoforms in response to stress and cell death induced by acetic acid. PLoS One *8*, e71294. https://doi.org/10.1371/journal.pone.0071294.
15. Magherini, F., Tani, C., Gamberi, T., Caselli, A., Bianchi, L., Bini, L., and Modesti, A. (2007). Protein expression profiles in Saccharomyces cerevisiae during apoptosis induced by H2O2. Proteomics *7*, 1434-1445. https://doi.org/10.1002/pmic.200600796.

16. Sousa, M., Duarte, A.M., Fernandes, T.R., Chaves, S.R., Pacheco, A., Leao, C., Corte-Real, M., and Sousa, M.J. (2013). Genome-wide identification of genes involved in the positive and negative regulation of acetic acid-induced programmed cell death in Saccharomyces cerevisiae. BMC Genomics *14*, 838. https://doi.org/10.1186/1471-2164-14-838.
17. Longo, V., Zdralevic, M., Guaragnella, N., Giannattasio, S., Zolla, L., and Timperio, A.M. (2015). Proteome and metabolome profiling of wild-type and YCA1-knock-out yeast cells during acetic acid-induced programmed cell death. J Proteomics *128*, 173-188. https://doi.org/10.1016/j.jprot.2015.08.003.
18. Teng, X., Dayhoff-Brannigan, M., Cheng, W.C., Gilbert, C.E., Sing, C.N., Diny, N.L., Wheelan, S.J., Dunham, M.J., Boeke, J.D., Pineda, F.J., and Hardwick, J.M. (2013). Genome-wide consequences of deleting any single gene. Mol Cell *52*, 485-494. https://doi.org/10.1016/j.molcel.2013.09.026.
19. Dong, Y., Hu, J., Fan, L., and Chen, Q. (2017). RNA-Seq-based transcriptomic and metabolomic analysis reveal stress responses and programmed cell death induced by acetic acid in Saccharomyces cerevisiae. Sci Rep *7*, 42659. https://doi.org/10.1038/srep42659.
20. Guo, T., Steen, J.A., and Mann, M. (2025). Mass-spectrometry-based proteomics: from single cells to clinical applications. Nature *638*, 901-911. https://doi.org/10.1038/s41586-025-08584-0.
21. Gillet, L.C., Navarro, P., Tate, S., Rost, H., Selevsek, N., Reiter, L., Bonner, R., and Aebersold, R. (2012). Targeted data extraction of the MS/MS spectra generated by data-independent acquisition: a new concept for consistent and accurate proteome analysis. Mol Cell Proteomics *11*, O111 016717. https://doi.org/10.1074/mcp.O111.016717.
22. Love, M.I., Huber, W., and Anders, S. (2014). Moderated estimation of fold change and dispersion for RNA-seq data with DESeq2. Genome Biol *15*, 550. https://doi.org/10.1186/s13059-014-0550-8.
23. Feng, Z., Fang, P., Zheng, H., and Zhang, X. (2023). DEP2: an upgraded comprehensive analysis toolkit for quantitative proteomics data. Bioinformatics *39*, btad526. https://doi.org/10.1093/bioinformatics/btad526.
24. Ludovico, P., Sousa, M.J., Silva, M.T., Leao, C.L., and Corte-Real, M. (2001). Saccharomyces cerevisiae commits to a programmed cell death process in response to acetic acid. Microbiology (Reading) *147*, 2409-2415. https://doi.org/10.1099/00221287-147-9-2409.
25. Grassl, J., Westbrook, J.A., Robinson, A., Boren, M., Dunn, M.J., and Clyne, R.K. (2009). Preserving the yeast proteome from sample degradation. Proteomics *9*, 4616-4626. https://doi.org/10.1002/pmic.200800945.
26. Kanshin, E., Tyers, M., and Thibault, P. (2015). Sample Collection Method Bias Effects in Quantitative Phosphoproteomics. J Proteome Res *14*, 2998-3004. https://doi.org/10.1021/acs.jproteome.5b00404.
27. Demichev, V., Messner, C.B., Vernardis, S.I., Lilley, K.S., and Ralser, M. (2020). DIA-NN: neural networks and interference correction enable deep proteome coverage in high throughput. Nat Methods *17*, 41-44. https://doi.org/10.1038/s41592-019-0638-x.
28. Yu, Y., Zhang, N., Mai, Y., Ren, L., Chen, Q., Cao, Z., Chen, Q., Liu, Y., Hou, W., Yang, J., et al. (2023). Correcting batch effects in large-scale multiomics studies using a reference-material-based ratio method. Genome Biol *24*, 201. https://doi.org/10.1186/s13059-023-03047-z.
29. Gasch, A.P., Spellman, P.T., Kao, C.M., Carmel-Harel, O., Eisen, M.B., Storz, G., Botstein, D., and Brown, P.O. (2000). Genomic expression programs in the response of yeast cells to environmental changes. Mol Biol Cell *11*, 4241-4257. https://doi.org/10.1091/mbc.11.12.4241.
30. Dong, J., Lai, R., Nielsen, K., Fekete, C.A., Qiu, H., and Hinnebusch, A.G. (2004). The essential ATP-binding cassette protein RLI1 functions in translation by promoting preinitiation complex assembly. J Biol Chem *279*, 42157-42168. https://doi.org/10.1074/jbc.M404502200.
31. Kispal, G., Sipos, K., Lange, H., Fekete, Z., Bedekovics, T., Janaky, T., Bassler, J., Aguilar Netz, D.J., Balk, J., Rotte, C., and Lill, R. (2005). Biogenesis of cytosolic ribosomes requires

the essential iron-sulphur protein Rli1p and mitochondria. EMBO J *24*, 589-598. https://doi.org/10.1038/sj.emboj.7600541.

32. Arenas, J.E., and Abelson, J.N. (1997). Prp43: An RNA helicase-like factor involved in spliceosome disassembly. Proc Natl Acad Sci U S A *94*, 11798-11802. https://doi.org/10.1073/pnas.94.22.11798.

33. Pfeffer, S., Woellhaf, M.W., Herrmann, J.M., and Forster, F. (2015). Organization of the mitochondrial translation machinery studied in situ by cryoelectron tomography. Nat Commun *6*, 6019. https://doi.org/10.1038/ncomms7019.

34. Gerashchenko, M.V., Lobanov, A.V., and Gladyshev, V.N. (2012). Genome-wide ribosome profiling reveals complex translational regulation in response to oxidative stress. Proc Natl Acad Sci U S A *109*, 17394-17399. https://doi.org/10.1073/pnas.1120799109.

35. Brauer, M.J., Huttenhower, C., Airoldi, E.M., Rosenstein, R., Matese, J.C., Gresham, D., Boer, V.M., Troyanskaya, O.G., and Botstein, D. (2008). Coordination of growth rate, cell cycle, stress response, and metabolic activity in yeast. Mol Biol Cell *19*, 352-367. https://doi.org/10.1091/mbc.e07-08-0779.

36. Chen, R.T., Rubanova, Y., Bettencourt, J., and Duvenaud, D.K. (2018). Neural ordinary differential equations. Advances in neural information processing systems *31*. https://doi.org/10.5555/3327757.3327764.

37. Mollapour, M., and Piper, P.W. (2007). Hog1 mitogen-activated protein kinase phosphorylation targets the yeast Fps1 aquaglyceroporin for endocytosis, thereby rendering cells resistant to acetic acid. Mol Cell Biol *27*, 6446-6456. https://doi.org/10.1128/MCB.02205-06.

38. Mollapour, M., and Piper, P.W. (2006). Hog1p mitogen-activated protein kinase determines acetic acid resistance in Saccharomyces cerevisiae. FEMS Yeast Res *6*, 1274-1280. https://doi.org/10.1111/j.1567-1364.2006.00118.x.

39. Ullah, A., Orij, R., Brul, S., and Smits, G.J. (2012). Quantitative analysis of the modes of growth inhibition by weak organic acids in Saccharomyces cerevisiae. Appl Environ Microbiol *78*, 8377-8387. https://doi.org/10.1128/AEM.02126-12.

40. Carmelo, V., Santos, H., and Sa-Correia, I. (1997). Effect of extracellular acidification on the activity of plasma membrane ATPase and on the cytosolic and vacuolar pH of Saccharomyces cerevisiae. Biochim Biophys Acta *1325*, 63-70. https://doi.org/10.1016/s0005-2736(96)00245-3.

41. Miller, E.W., Dickinson, B.C., and Chang, C.J. (2010). Aquaporin-3 mediates hydrogen peroxide uptake to regulate downstream intracellular signaling. Proc Natl Acad Sci U S A *107*, 15681-15686. https://doi.org/10.1073/pnas.1005776107.

42. Halliwell, B., and Aruoma, O.I. (1991). DNA damage by oxygen-derived species. Its mechanism and measurement in mammalian systems. FEBS Lett *281*, 9-19. https://doi.org/10.1016/0014-5793(91)80347-6.

43. Perrone, G.G., Tan, S.X., and Dawes, I.W. (2008). Reactive oxygen species and yeast apoptosis. Biochim Biophys Acta *1783*, 1354-1368. https://doi.org/10.1016/j.bbamcr.2008.01.023.

44. Evans, M.V., Turton, H.E., Grant, C.M., and Dawes, I.W. (1998). Toxicity of linoleic acid hydroperoxide to Saccharomyces cerevisiae: involvement of a respiration-related process for maximal sensitivity and adaptive response. J Bacteriol *180*, 483-490. https://doi.org/10.1128/JB.180.3.483-490.1998.

45. Sena, L.A., and Chandel, N.S. (2012). Physiological roles of mitochondrial reactive oxygen species. Mol Cell *48*, 158-167. https://doi.org/10.1016/j.molcel.2012.09.025.

46. Olsen, J.V., and Mann, M. (2013). Status of large-scale analysis of post-translational modifications by mass spectrometry. Mol Cell Proteomics *12*, 3444-3452. https://doi.org/10.1074/mcp.O113.034181.

47. Huffman, R.G., Leduc, A., Wichmann, C., Di Gioia, M., Borriello, F., Specht, H., Derks, J., Khan, S., Khoury, L., Emmott, E., et al. (2023). Prioritized mass spectrometry increases the depth, sensitivity and data completeness of single-cell proteomics. Nat Methods *20*, 714-722. https://doi.org/10.1038/s41592-023-01830-1.

48. Gao, H., Zhang, F., Liang, S., Zhang, Q., Lyu, M., Qian, L., Liu, W., Ge, W., Chen, C., Yi, X., et al. (2020). Accelerated Lysis and Proteolytic Digestion of Biopsy-Level Fresh-Frozen and FFPE Tissue Samples Using Pressure Cycling Technology. J Proteome Res *19*, 1982-1990. https://doi.org/10.1021/acs.jproteome.9b00790.
49. Cai, X., Xue, Z., Wu, C., Sun, R., Qian, L., Yue, L., Ge, W., Yi, X., Liu, W., Chen, C., et al. (2022). High-throughput proteomic sample preparation using pressure cycling technology. Nat Protoc *17*, 2307-2325. https://doi.org/10.1038/s41596-022-00727-1.
50. Bruderer, R., Bernhardt, O.M., Gandhi, T., Miladinovic, S.M., Cheng, L.Y., Messner, S., Ehrenberger, T., Zanotelli, V., Butscheid, Y., Escher, C., et al. (2015). Extending the limits of quantitative proteome profiling with data-independent acquisition and application to acetaminophen-treated three-dimensional liver microtissues. Mol Cell Proteomics *14*, 1400-1410. https://doi.org/10.1074/mcp.M114.044305.
51. Bolstad, B.M. (2013). preprocessCore: A collection of pre-processing functions. R package version *1*, 2. https://doi.org/10.18129/B9.bioc.preprocessCore.
52. Johnson, W.E., Li, C., and Rabinovic, A. (2007). Adjusting batch effects in microarray expression data using empirical Bayes methods. Biostatistics *8*, 118-127. https://doi.org/10.1093/biostatistics/kxj037.
53. Zhang, Y., Parmigiani, G., and Johnson, W.E. (2020). ComBat-seq: batch effect adjustment for RNA-seq count data. NAR Genom Bioinform *2*, lqaa078. https://doi.org/10.1093/nargab/lqaa078.
54. Smyth, G.K., and Speed, T. (2003). Normalization of cDNA microarray data. Methods *31*, 265-273. https://doi.org/10.1016/s1046-2023(03)00155-5.
55. Zhang, S. (2012). Nearest neighbor selection for iteratively kNN imputation. Journal of Systems and Software *85*, 2541-2552. https://doi.org/https://doi.org/10.1016/j.jss.2012.05.073.
56. Shannon, C.E. (1949). Communication in the Presence of Noise. Proceedings of the IRE *37*, 10-21. https://doi.org/10.1109/JRPROC.1949.232969.
57. Conesa, A., Nueda, M.J., Ferrer, A., and Talón, M. (2006). maSigPro: a method to identify significantly differential expression profiles in time-course microarray experiments. Bioinformatics *22*, 1096-1102. https://doi.org/10.1093/bioinformatics/btl056.
58. Langfelder, P., and Horvath, S. (2008). WGCNA: an R package for weighted correlation network analysis. BMC Bioinformatics *9*, 559. https://doi.org/10.1186/1471-2105-9-559.
59. Wu, T., Hu, E., Xu, S., Chen, M., Guo, P., Dai, Z., Feng, T., Zhou, L., Tang, W., Zhan, L., et al. (2021). clusterProfiler 4.0: A universal enrichment tool for interpreting omics data. Innovation (Camb) *2*, 100141. https://doi.org/10.1016/j.xinn.2021.100141.
60. Chung, J., Gulcehre, C., Cho, K., and Bengio, Y. (2014). Empirical evaluation of gated recurrent neural networks on sequence modeling. arXiv preprint arXiv:1412.3555. https://doi.org/10.48550/arXiv.1412.3555.

Acknowledgements

This work is supported by grants from Joint Funds of the National Natural Science Foundation of China (No. U24A20476), National Natural Science Foundation of China (Young Scientist Fund, No. 32401239), the Zhejiang Provincial Natural Science Foundation of China (LQ24C050002), Pioneer and Leading Goose R&D Program of Zhejiang (2024SSYS0035), National Key R&D Program of China (No. 2022YFF0608403, 2021YFA1301600), and the State Key Laboratory of Medical Proteomics (SKLP-Y202403).

Author contributions

T.G. conceived the project, supervised the study, and provided overall direction. Z.Z. designed the specific experimental workflows, performed the time-series sample collection and proteomic profiling, developed the computational pipeline (including clustering, GAMs, and Neural ODEs), analyzed the data, generated all figures, and wrote the original draft of the manuscript. R.S. provided critical insights and significantly revised the manuscript. Z.L. contributed to the optimization of experimental protocols and assisted with pilot experiments. S.W. performed the DIA spectral library search, and assisted with time-series sampling. Z.D. assisted with sample collection. L.Z. was responsible for mass spectrometry instrument operation and data acquisition. K.M. and G.Z. assisted with sample preparation. L.Q. contributed to data interpretation and helpful discussions.

Declaration of interests

T.G. is the shareholder of Westlake Omics (Hangzhou) Biotechnology Co., Ltd. The other authors declare no competing interests.

Figure 1

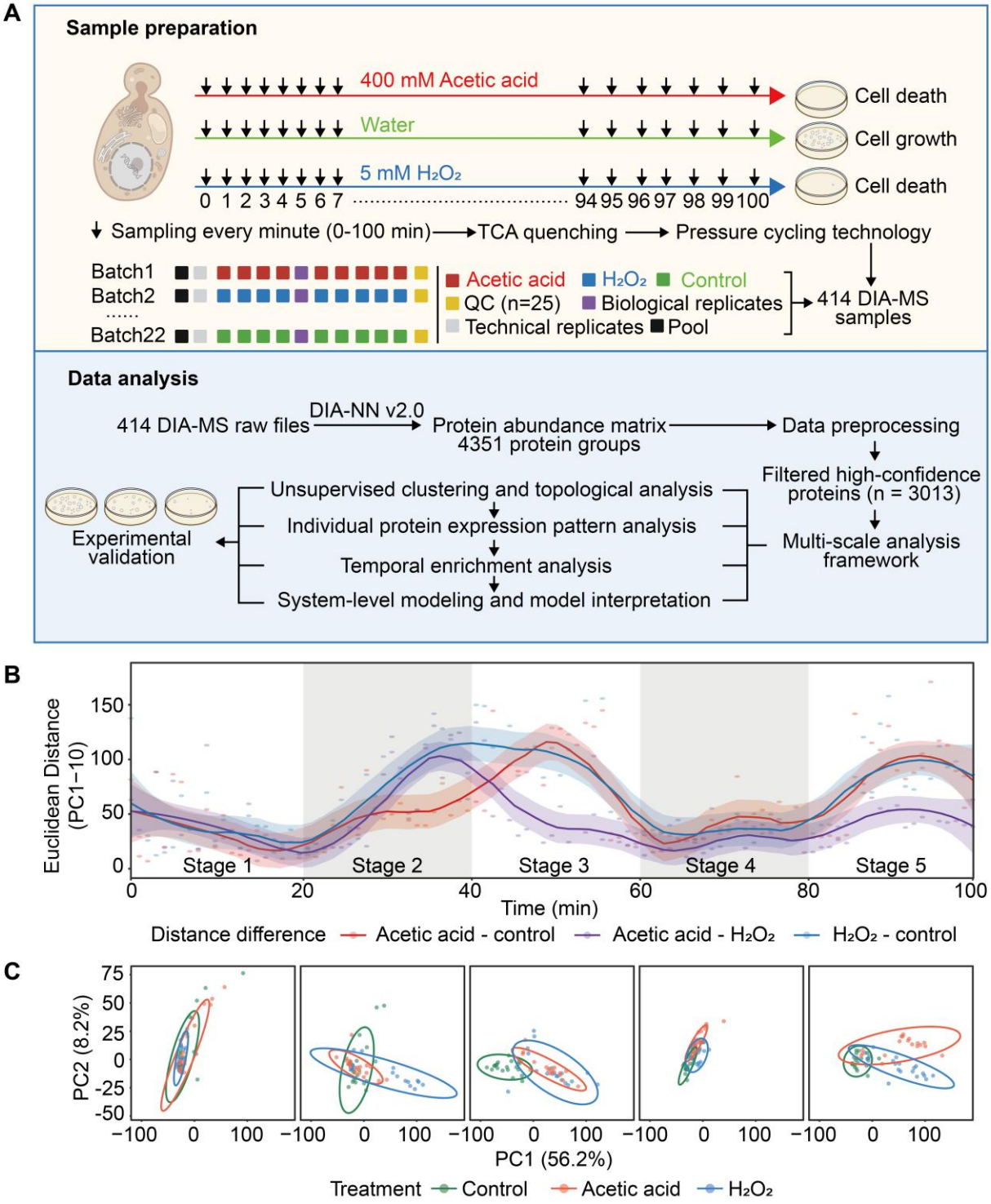

Figure 1 | High-resolution temporal proteomic profiling reveals the dynamic divergence of yeast cell death trajectories. **(A)** Schematic of the Proteome video experimental and computational framework. *S. cerevisiae* cultures were subjected to lethal doses of acetic acid (400 mM, red) or hydrogen peroxide (5 mM, blue), with water as a control (green). Samples were collected at 1-minute intervals over a 100-minute time course. The pipeline integrates high-frequency DIA-MS (quantifying 4351 protein groups) with a multi-scale analytical framework, ranging from unsupervised clustering to system-level Neural ODE modeling and experimental validation. **(B)** Quantification of dynamic

proteome divergence. The plot displays the temporal evolution of Euclidean distances between group centroids within the space of the first ten principal components (PC1-10). Curves represent the distance difference between stress conditions and control (Red: Acetic acid vs. Control; Blue: H_2O_2 vs. Control) and between the two lethal conditions (Purple: Acetic acid vs. H_2O_2). Shaded areas indicate 95% confidence intervals. The trajectory is segmented into five distinct kinetic stages (Stage 1–5) based on the divergence patterns. **(C)** Phase-specific Principal Component Analysis. Snapshots of the proteomic state space (PC1 vs. PC2) corresponding to the five temporal stages defined in (B). Ellipses represent 95% confidence intervals. The plots visualize the progression from an initial latent phase (Stage 1) to a clear bifurcation and subsequent divergence of stress-specific trajectories.

Figure 2

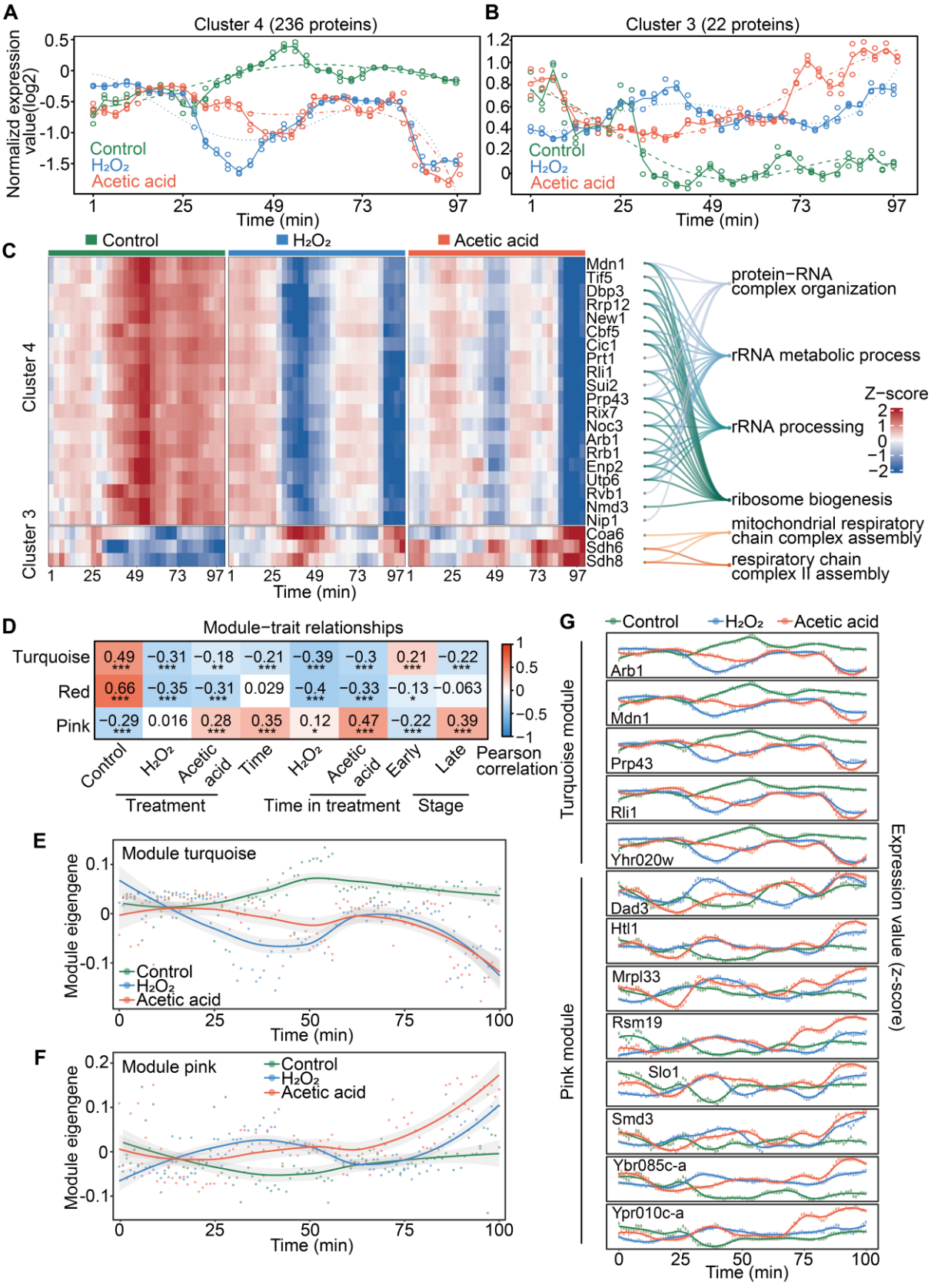

Figure 2 | Shared and stress-specific proteomic programs orchestrate cellular responses to lethal stress. (A, B) Temporal clustering (maSigPro) identifies distinct kinetic patterns shared across

conditions or specific to stress responses. **(A)** Cluster 4 (n=236 proteins) reflects a conserved growth arrest program, while **(B)** Cluster 3 (n=22 proteins) represents a shared stress-responsive upregulation program. **(C)** Detailed visualization of representative proteins and their functional connections. The heatmap displays the temporal expression profiles (z-scored) of the top 20 proteins with the highest goodness-of-fit (R2) to the centroids of Cluster 4 (top) and Cluster 3 (bottom). The right panel utilizes a ribbon plot to map these individual proteins (e.g., Mdn1, Rli1 in Cluster 4; Coa6, Sdh6 in Cluster 3) directly to their enriched Gene Ontology (GO) biological processes, illustrating the molecular basis of ribosome biogenesis suppression and mitochondrial respiratory chain assembly, respectively. **(D)** Weighted Gene Co-expression Network Analysis (WGCNA) module-trait relationships. The heatmap shows the correlation between module eigengenes and experimental traits. The Turquoise module (n=779) correlates positively with the Control state, while the Pink module (n=8) shows a specific strong positive correlation with Acetic Acid treatment. **(E, F, G)** Resolving module dynamics at the eigengene and single-protein level. **(E, F)** Longitudinal trajectories of the Turquoise **(E)** and Pink **(F)** module eigengenes (shaded areas indicate 95% confidence intervals). **(G)** Representative abundance traces of individual hub proteins within these modules. The Turquoise module (e.g., Arb1, Prp43) mirrors the global growth arrest trend, while the Pink module reveals an acetic acid-specific upregulation of mitochondrial ribosome components (e.g., Mrpl33, Rsm19), highlighting a unique mitochondrial related strategy that operates independently of the global cytosolic shutdown.

Figure 3

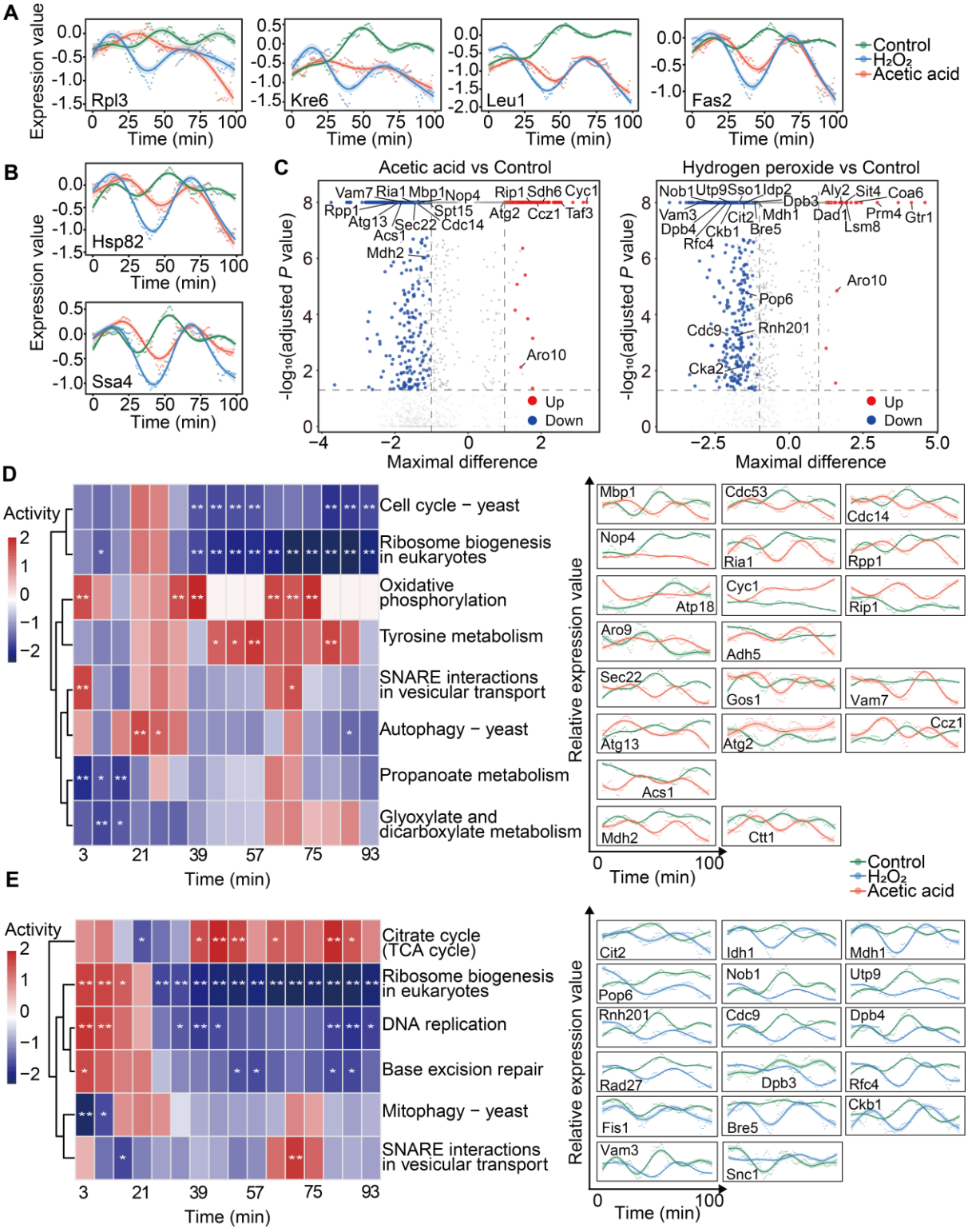

Figure 3 | High-resolution kinetics resolve intrinsic homeostatic oscillations and divergent execution landscapes of yeast cell death. **(A, B)** Generalized Additive Model (GAM) fitted trajectories of representative proteins. Curves represent the smooth trend of protein abundance over time (shaded areas indicate 95% confidence intervals). Trajectories are colored by condition: Control (green), Acetic Acid (red), and H2O2 (blue). **(A)** Canonical stress markers (e.g., Rpl3, Kre6) display rapid, monotonic downregulation, validating the capture of physiological growth arrest. **(B)**

Chaperones (Hsp82, Ssa4) exhibit complex oscillatory dynamics (transient induction followed by collapse); this demonstrates the framework's ability to resolve non-linear behaviors obscured in static snapshots. **(C)** Kinetic Volcano Plots for the identification of dynamic responders. The x-axis represents the Maximal Difference (MaxDiff) between stress and control trajectories, serving as a temporal proxy for response magnitude. The y-axis displays statistical significance (-log10 adjusted *P*-value). Colored points highlight proteins that are both statistically significant and exhibit sustained dynamic changes (filtered by ranking in the top 50% of Root Mean Square Deviation, RMSD). Key proteins functioning as drivers in specific pathways (analyzed in D and E) are explicitly labeled. **(D, E)** Time-resolved functional landscapes and corresponding single-protein kinetics. Left: Heatmaps visualize the temporal evolution of pathway activity (GSEA) based on GAM-derived binned AUC scores. Color intensity represents the Normalized Enrichment Score (NES) (Red: activated/upregulated; Blue: suppressed/downregulated). Significance is denoted by asterisks (* $P<0.05$, ** $P<0.01$). Right: Representative GAM-fitted trajectories of core proteins from the highlighted pathways, confirming that pathway-level NES trends are driven by specific protein abundance changes. Trajectories are colored by condition: Control (green), Acetic Acid (red), and H2O2 (blue). **(D)** Acetic acid-induced RCD is characterized by a metabolic exhaustion program, showing the upregulation of Oxidative phosphorylation (Atp18, Rip1) and SNARE interactions (Sec22, Vam7) amidst metabolic suppression (Acs1, Mdh2). **(E)** Hydrogen peroxide-induced RCD triggers a genomic triage cascade, defined by the robust, prioritized activation of DNA replication and Base excision repair (Rnh201, Rad27, Rfc4) contrasting with the suppression of Mitophagy (Fis1,Vam3).

Figure 4

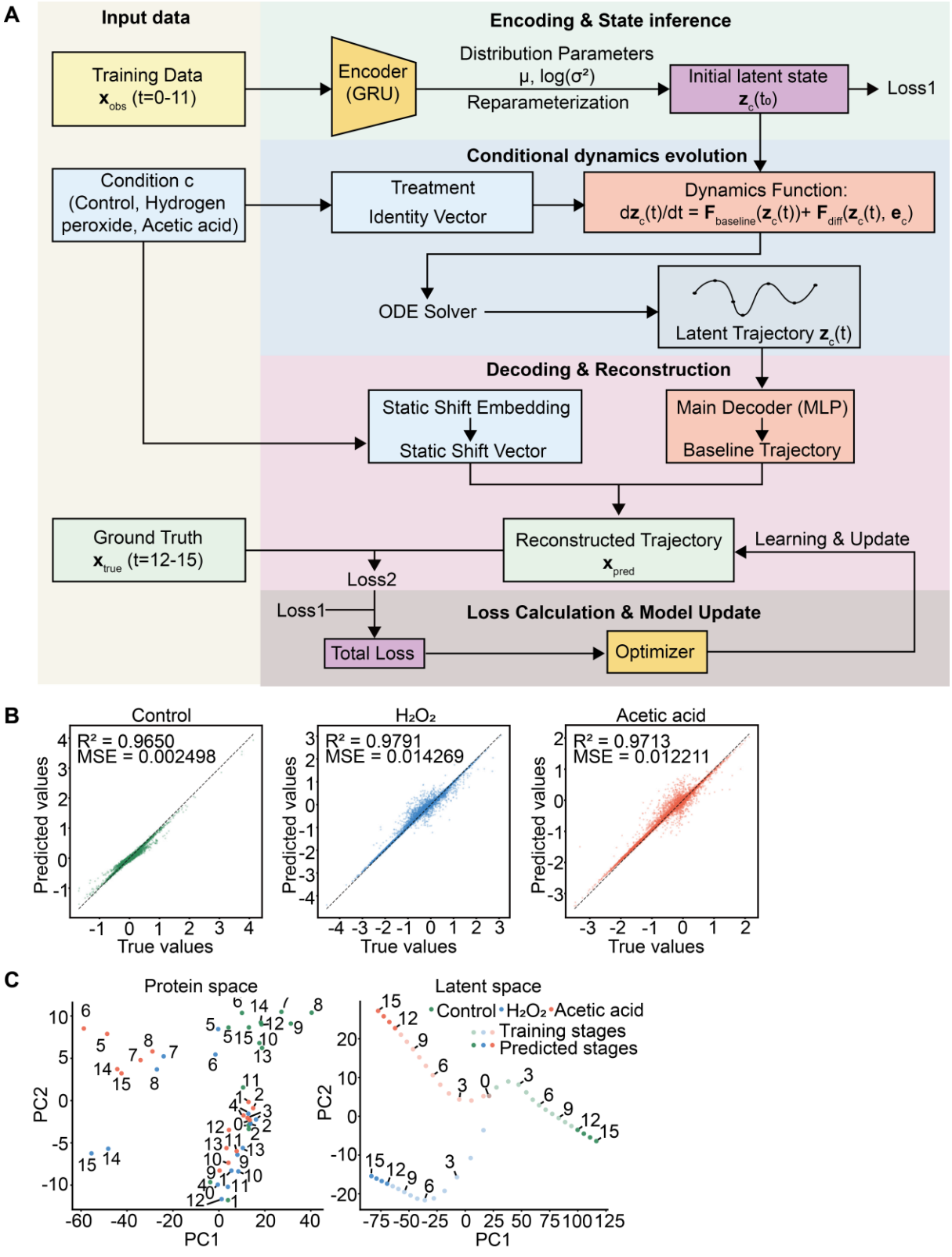

Figure 4 | Learning continuous proteome dynamics to infer upstream drivers of cell death subroutines. (**A**) Architecture of the framework. The model is designed to learn a continuous, low-dimensional representation of proteome evolution from discrete time-series data. Observed snapshots ($\mathbf{X}_{\text{obs}}$) are encoded into an initial latent state ($\mathbf{z}_{t_0}$). The system's evolution is governed by a learnable

ODE, where the time derivative ($\frac{d\mathbf{z}_c(t)}{dt}$) is explicitly decomposed into a shared baseline field ($\mathbf{F}_{\text{baseline}}(\mathbf{z}_c(t))$) and a condition-specific perturbation field ($\mathbf{F}_{\text{diff}}(\mathbf{z}_c(t), \mathbf{e}_c)$). This structural constraint mathematically disentangles universal trends from stress-specific dynamic drivers. Crucially, the model is trained via a generative reconstruction task to enforce the learning of underlying evolutionary rules rather than simple interpolation. **(B)** Reconstruction fidelity. Scatter plots compare model-reconstructed protein abundances against ground truth values. High coefficients of determination ($R^2 > 0.96$) across all conditions confirm that the model accurately captures the complex, non-linear variability of the proteome. **(C)** Denoising and manifold learning. Comparative PCA of the raw proteome data (left) versus the learned latent space (right). While raw data exhibit stochastic noise (jagged trajectories), the latent manifold reveals smooth, continuous evolutionary paths. Semi-transparent dots correspond to the encoded observation steps (training), while opaque dots represent the reconstructed future states, demonstrating the model has successfully extracted the governing biological signal from high-frequency noise, creating a biologically meaningful dynamical landscape.

Figure 5

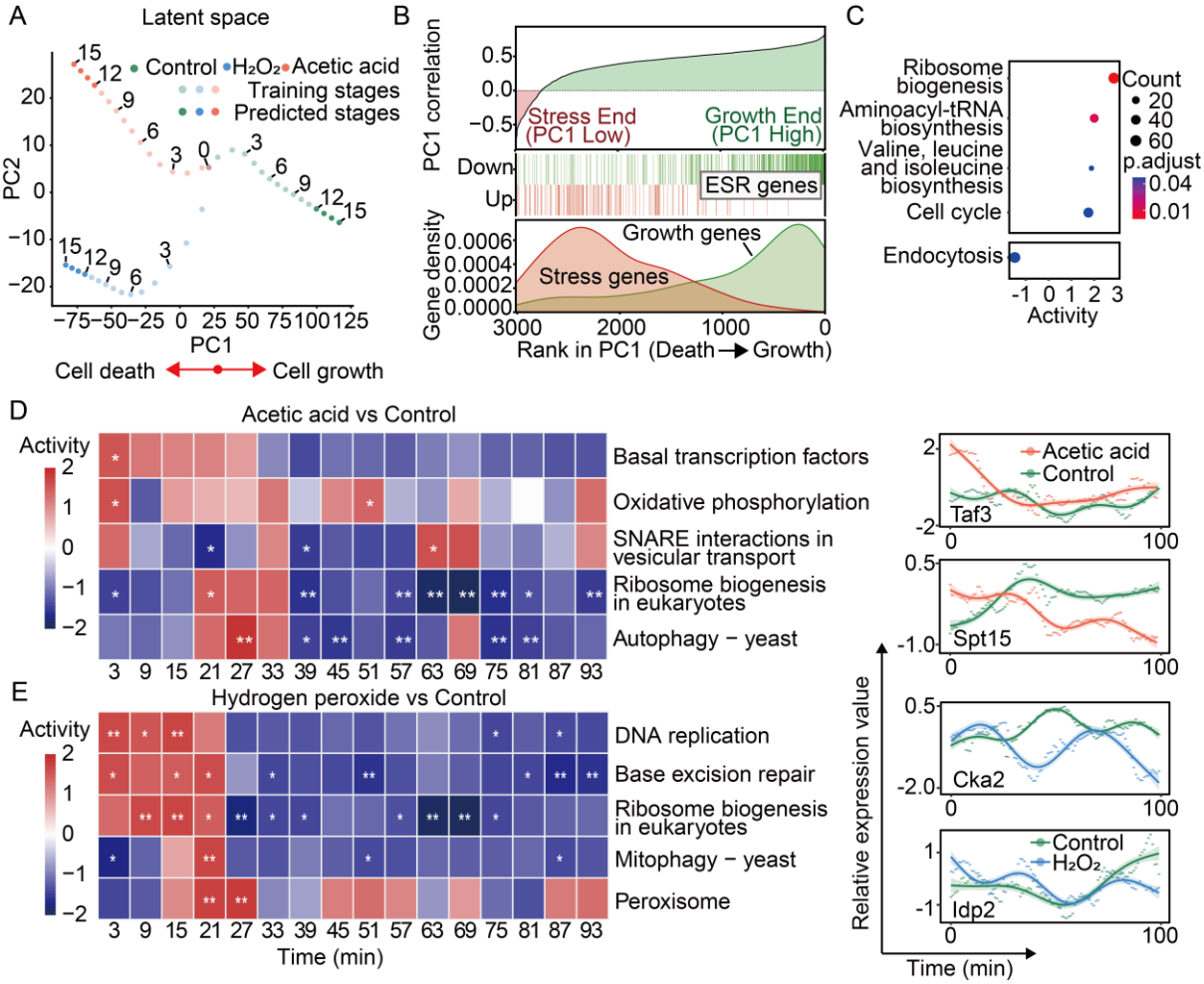

Figure 5 | Validation of the latent space geometry and unsupervised discovery of temporal drivers via gradient analysis. (A) PCA projection of the learned latent trajectories ($z_{(t)}$). The model autonomously organizes the proteome along a dominant Growth-Death axis (PC1, 90.7% variance), reconstructing the topological transition from homeostasis (green) to stress-induced collapse (red/blue) without prior biological labels. **(B, C)** Biological validation of the latent axis. **(B)** Proteins positively correlated with PC1 (Growth end) are significantly enriched in ESR-Repressed genes, while negatively correlated proteins (Death end) enrich in ESR-Induced genes. **(C)** GSEA of proteins ranked by their correlation with PC1 scores confirms that the axis captures the transition from ribosome biogenesis to endocytosis-mediated membrane remodeling. **(D)** Time-resolved Signed Saliency heatmaps identifying upstream drivers of system evolution. Unlike abundance measures, high saliency denotes proteins that actively determine the future trajectory. Acetic acid (Top): Gradient analysis reveals the Basal transcription factors pathway as the primary initiating driver (active at 3 min), temporally preceding the execution of the oxidative phosphorylation defense. H_2O_2 (Bottom): The analysis uncovers a transient rescue signal at 21 minutes marked by the synchronized activation of Mitophagy and Peroxisome pathways—a critical regulatory event missed by conventional abundance profiling. **(E)** Abundance trajectories of representative drivers identified by the gradient analysis. Taf3 and Spt15 (Basal TFs) display early-phase dynamics in response to acetic acid. In the H_2O_2 condition, Cka2 and Idp2 (cytosolic NADP-specific isocitrate dehydrogenase) are identified as key effectors of the 21-minute rescue attempt, with Idp2 upregulation suggesting a mechanism for NADPH production to support ROS clearance. Trajectories are colored by condition: Control (green), Acetic Acid (red), and H_2O_2 (blue).

Figure 6

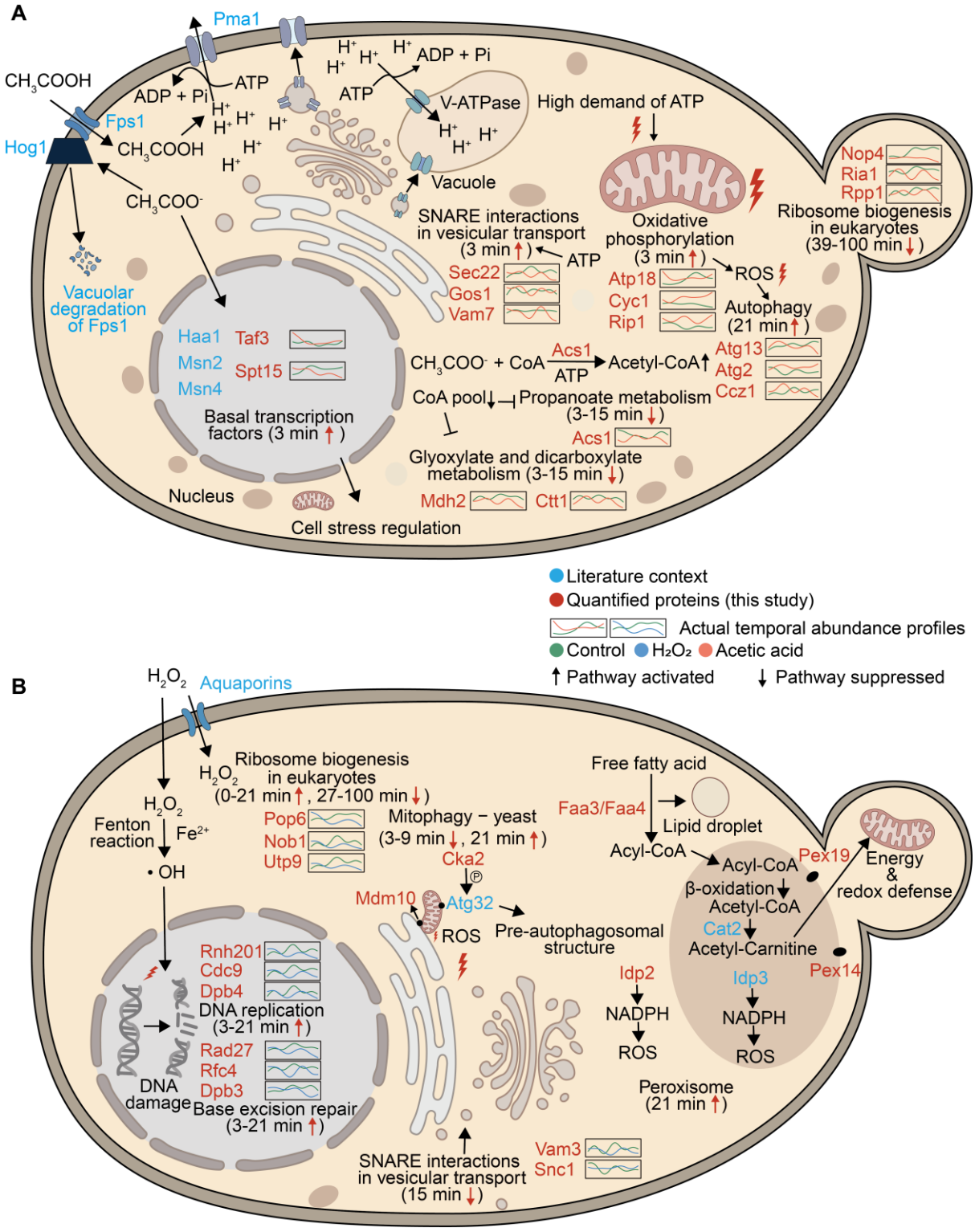

Figure 6 | Hypothetical systems view of the integrated molecular landscapes driving yeast cell death. Schematic reconstruction of the chronological molecular events driving (A) Acetic acid-induced metabolic exhaustion and (B) Hydrogen peroxide-induced genomic triage. Color coding: Blue indicates mechanisms established in prior literature; Red indicates novel kinetic drivers and regulatory events identified in this study via high-frequency proteomics and Neural ODE gradient analysis; Yellow indicates findings consistent between literature and our data. **(A)** Acetic Acid Landscape.

Following acetate entry (regulated by Fps1/Hog1), the response is initiated by Basal Transcription Factors (Taf3, Spt15, 3 min), identified here as early drivers preceding canonical stress signaling. The subsequent Active Defense phase (3–15 min) involves robust Oxidative Phosphorylation and SNARE-mediated proton pump trafficking to counteract acidification. Mechanistically, the conversion of acetate to acetyl-CoA may deplete the cytosolic CoA pool, leading to the specific suppression of CoA-dependent pathways (Propanoate/Glyoxylate metabolism). The sustained metabolic strain ultimately triggers a lethal Autophagy signal (Point of No Return, 21 min) followed by ribosomal collapse. **(B)** Hydrogen Peroxide Landscape. H_2O_2-derived hydroxyl radicals trigger a DNA Triage phase (0–21 min), prioritizing DNA replication and Base Excision Repair. Crucially, Mitophagy is suppressed during this early phase, creating a potential positive feedback loop where accumulating damaged mitochondria amplify ROS production. At 21 minutes, the system mounts a synchronized Rescue Attempt to break this cycle. This involves not only the activation of quality control via Cka2 (Mitophagy) and antioxidant defense via Idp2 (Peroxisomal NADPH), but also a specific metabolic rewiring mediated by Faa3 and Yat1. We interpret the latter as an emergency effort to shunt fatty acids into acetyl-carnitine, likely to refuel mitochondria or bypass cytosolic metabolic blocks. The ultimate failure of this multi-pronged rescue to contain the ROS cascade leads to terminal nuclear fragmentation and cell death.

Figure 7

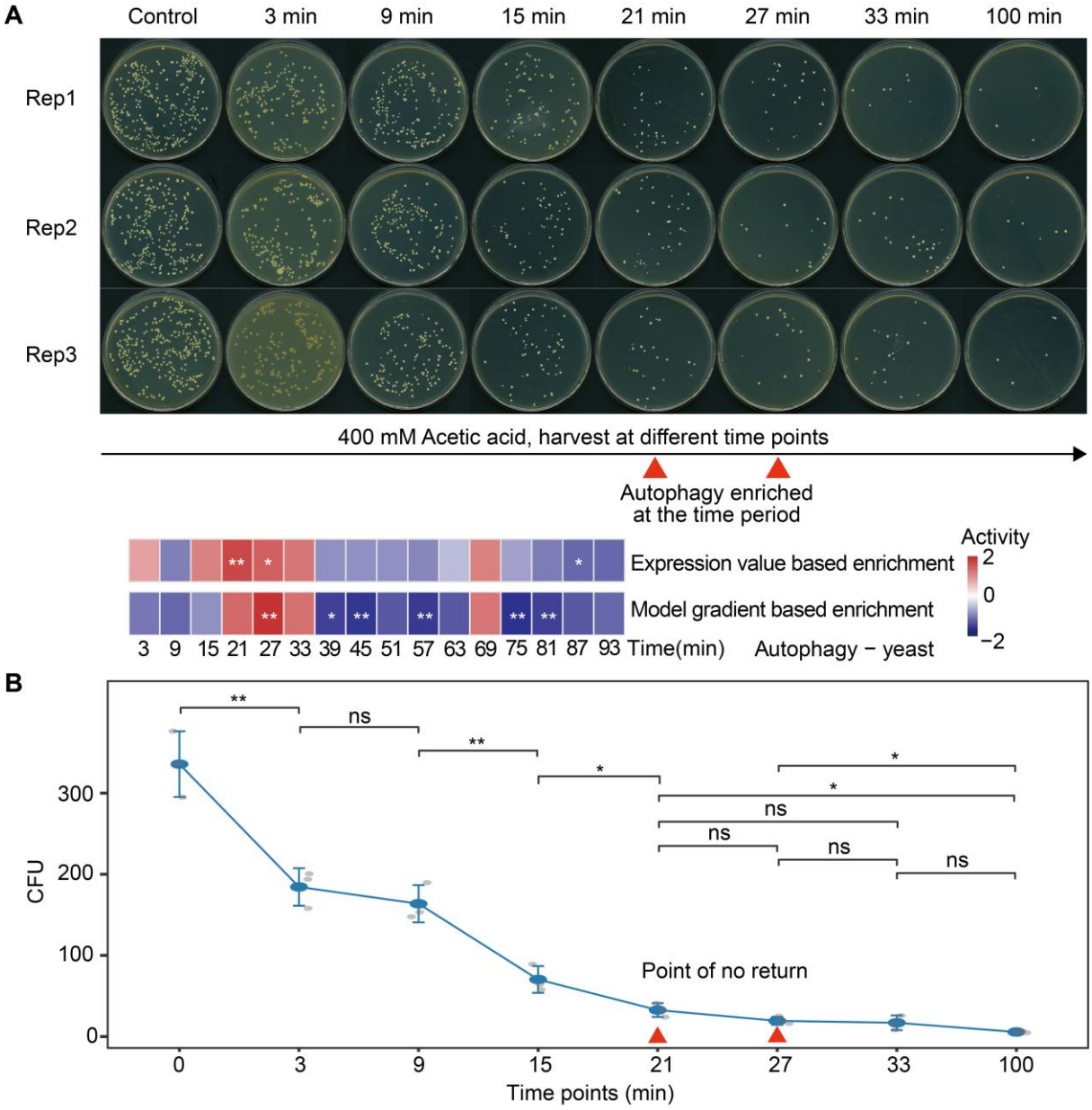

Figure 7 | Phenotypic anchoring of model-inferred drivers to the irreversible transition of cell fate. (A, B) Determination of the biological Point of No Return and its temporal alignment with model predictions. **(A)** Top: Representative images of clonogenic survival assays. Yeast cultures were exposed to 400 mM acetic acid, and at the indicated time points (0–100 min), aliquots were immediately harvested, washed twice with PBS to remove the stressor, and plated on YPD agar (n=3 biological replicates). Bottom: Temporal enrichment strips comparing the activation of the Autophagy pathway derived from abundance-based analysis (Top strip, GAM) versus gradient-based driver analysis (Bottom strip, Neural ODE). Notably, both methods identify the engagement of autophagy in the 21–27 minute window, synchronizing the regulatory signal with the onset of phenotypic collapse. **(B)** Quantification of Colony Forming Units (CFU) from the assay in (A). Statistical significance was assessed via pairwise comparisons using unpaired two-sided Welch's t-tests (* P<0.05, ** P<0.01, ns: not significant). The survival curve reveals a critical transition: a significant loss of viability occurs between 15 and 21 minutes ($P < 0.05$), after which lethality plateaus (no significant difference between 21, 27, and 33 min). We define this 21-minute mark as the Point of No Return, which temporally aligns with the abundance and gradient-inferred autophagy pulse.

Extended Figure 1

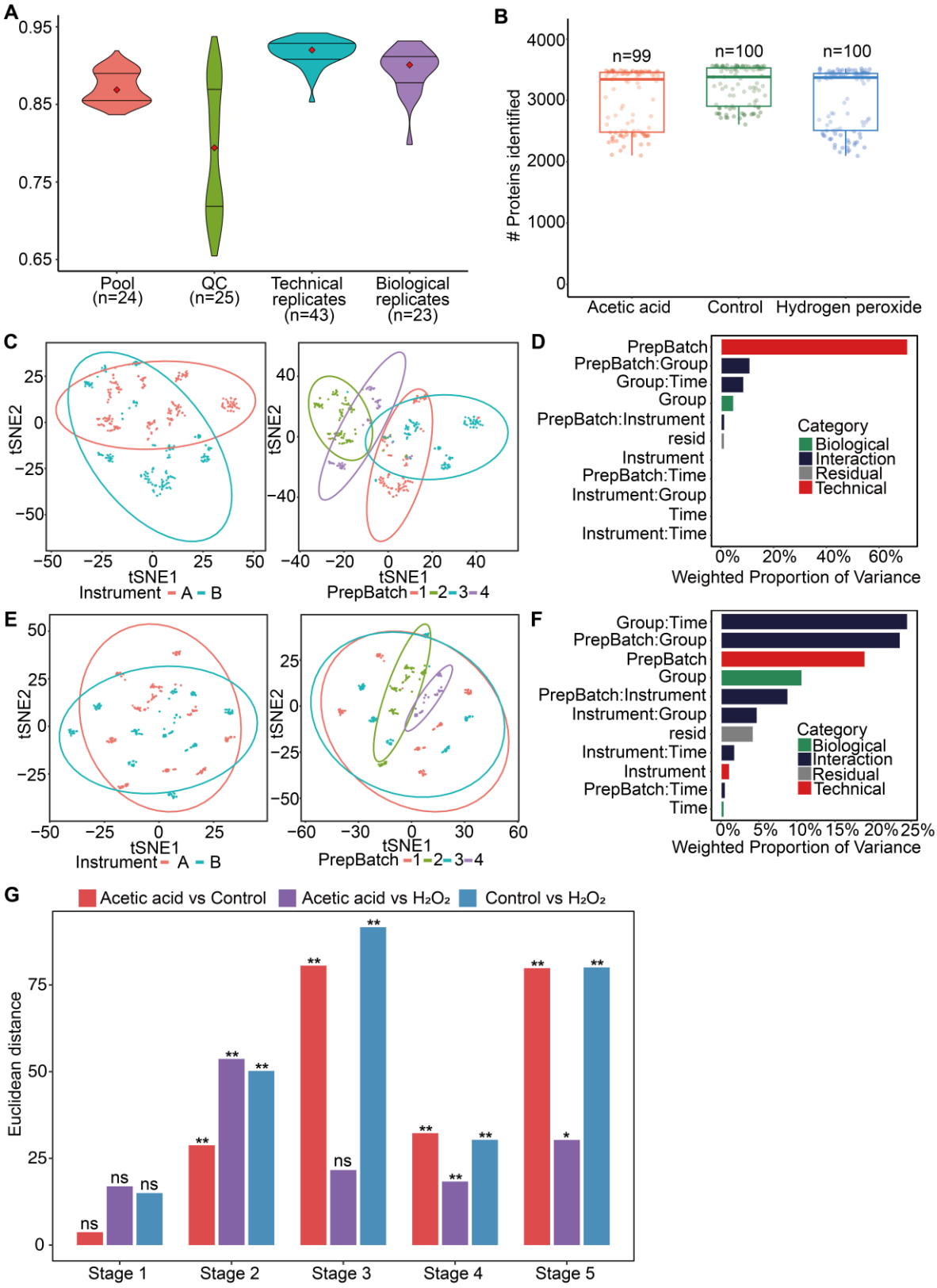

Extended Figure 1 | Data quality control, batch effect correction, and stage-specific quantification of proteome divergence. (A) High reproducibility of the proteomic data. Violin plots show the Pearson correlation coefficients for technical and biological replicates, both demonstrating high concordance. (**B**) Consistent proteome depth across experimental conditions. Boxplots show the

number of proteins identified per sample for each treatment group. (**C, D**) Visualization and quantification of batch effects before correction. (**C**) t-SNE plots show significant sample clustering by both instrument (left) and preparation batch (right). (**D**) Principal Variance Component Analysis (PVCA) confirms that technical factors (red bars), particularly preparation batch, account for the largest proportion of variance in the raw data. (**E, F**) Successful removal of batch effects after correction. (**E**) Post-correction t-SNE plots show that technical clustering is largely eliminated. (**F**) Post-correction PVCA demonstrates that biological factors (blue and green bars), especially the interaction between treatment group and time ("Group:Time"), now account for the majority of the variance, confirming the successful recovery of the underlying biological signal. (**G**) Stage-specific quantification of proteome divergence. The bar chart displays the Euclidean distance in the first ten principal components space between group centroids across five temporal stages (Significance: ns, not significant; *, $P < 0.05$; **, $P < 0.01$; assessed via PERMANOVA). The analysis reveals a latent phase (Stage 1), followed by peak divergence of stress trajectories from the control (Stage 2). Notably, the distance between the two lethal trajectories (Acetic acid vs H_2O_2, purple bars) significantly contracts during Stage 3, indicating a transient convergence, before a secondary divergence in the terminal stages (Stages 4 and 5).

Extended Figure 2

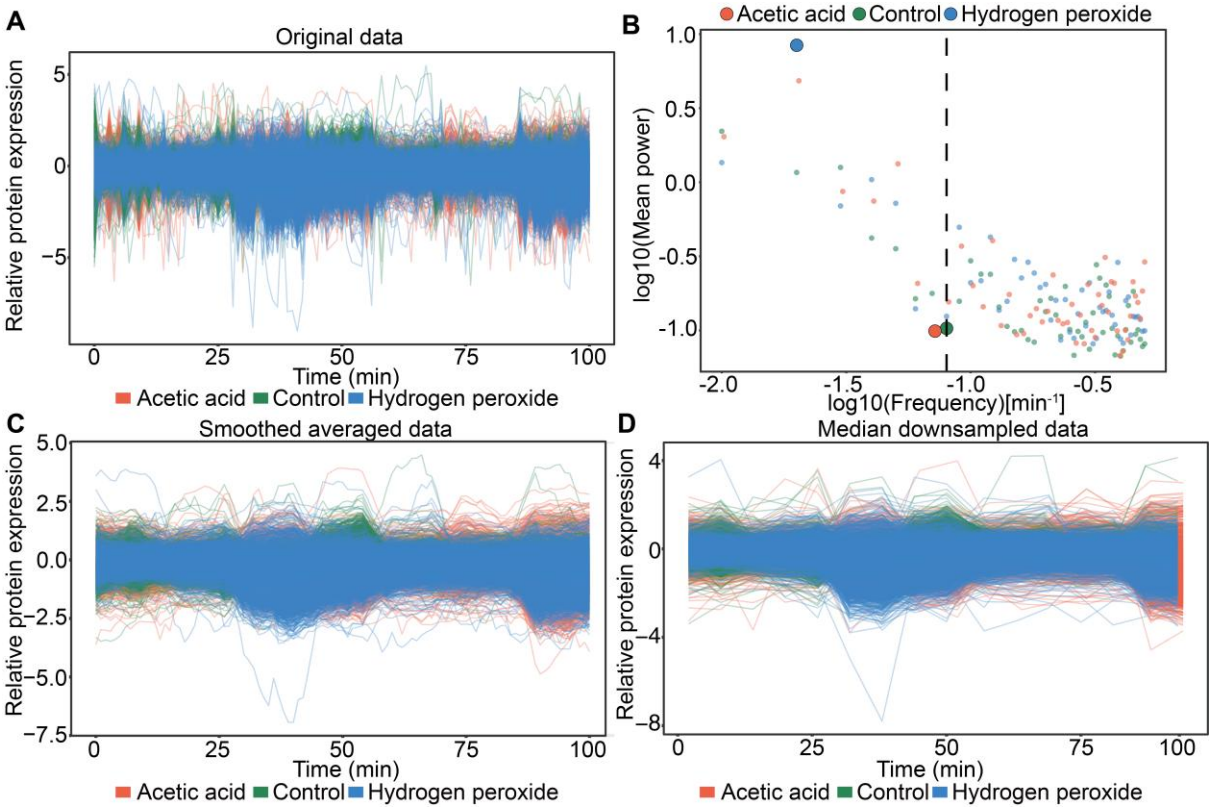

Extended Figure 2 | Frequency-domain analysis and signal denoising of high-resolution proteomic data. (**A**) Time-series profiles of all quantified proteins from the original data, illustrating the presence of high-frequency stochastic noise that can obscure underlying biological trends. (**B**) Identification of an optimal cutoff frequency using spectral analysis. The plot shows the Power Spectral Density (PSD) versus frequency for all proteins. An optimal cutoff frequency (dashed line, ~0.08 min^{-1}) was determined using the "Elbow Method", effectively separating the low-frequency biological signal from the high-frequency noise floor. This cutoff corresponds to a temporal window of approximately 6 minutes, as derived from the Nyquist-Shannon sampling theorem. (**C, D**) Generation of two distinct denoised datasets based on the calculated 6-minute window. (**C**) The smoothed dataset, generated by a 6-point moving average, retains the original temporal density (100 time points) and is used for trend-fitting analyses (e.g., GAM, WGCNA). (**D**) The downsampled dataset, generated by median binning into 16 six-minute intervals, aligns the data granularity with the biological timescale of protein-level regulation and is used for dynamic system modeling (Neural ODE).

Extended Figure 3

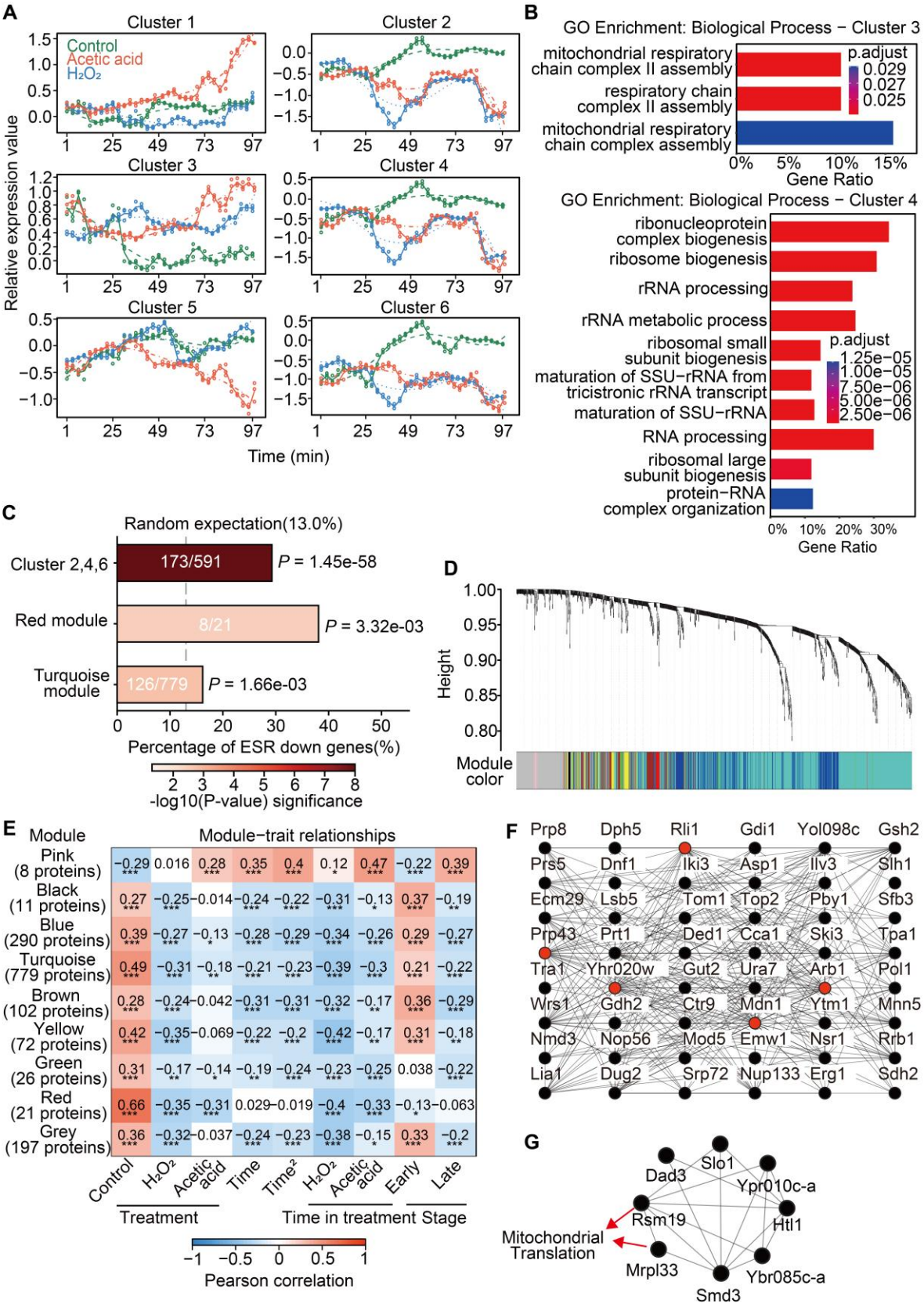

Extended Figure 3 | Comprehensive characterization of temporal proteomic patterns and functional network modules. (A) Complete temporal profiles of the six protein clusters identified by maSigPro analysis. Curves represent the median expression of all proteins within each cluster across

Control (green), Acetic Acid (red), and H_2O_2 (blue) conditions. Cluster 4 and Cluster 3 represent the dominant growth arrest (downregulated) and stress defense (upregulated) modes, respectively. **(B)** Gene Ontology (GO) enrichment analysis of the key clusters shown in (A). Cluster 3 is enriched in mitochondrial respiratory chain assembly, while Cluster 4 is enriched in ribosome biogenesis and rRNA processing, providing the functional basis for the Growth vs. Defense dichotomy. **(C)** External validation against the transcriptional Environmental Stress Response (ESR). Bar charts show the percentage of genes in the proteomic clusters (2, 4, 6) or WGCNA modules (Red, Turquoise) that overlap with the canonical ESR-Repressed gene set defined by Gasch et al. The highly significant overlap (*P* values from Fisher's exact test) confirms that the defined growth arrest programs are biologically consistent with established stress response signatures. **(D)** WGCNA clustering dendrogram. Proteins are grouped based on topological overlap in co-expression patterns, with assigned modules indicated by the color bar at the bottom. **(E)** Module-trait relationship heatmap. Values represent the Pearson correlation between module eigengenes (MEs) and experimental traits (Condition, Time). The Turquoise module is strongly associated with the homeostatic state (Control), while the Pink module shows a specific positive correlation with Acetic Acid treatment. **(F, G)** Topological visualization of key functional modules. Nodes represent proteins and edges represent high topological overlap (co-expression strength). **(F)** The Turquoise module forms a dense growth engine network comprising cytosolic translation and nucleotide synthesis machinery, with Rli1 and Prs5 identified as high-connectivity hubs. **(G)** The Pink module reveals a specialized network of mitochondrial ribosomal proteins (e.g., Mrpl33, Rsm19) specifically induced under acetic acid stress, indicating a distinct mitochondrial translation program.

Extended Figure 4

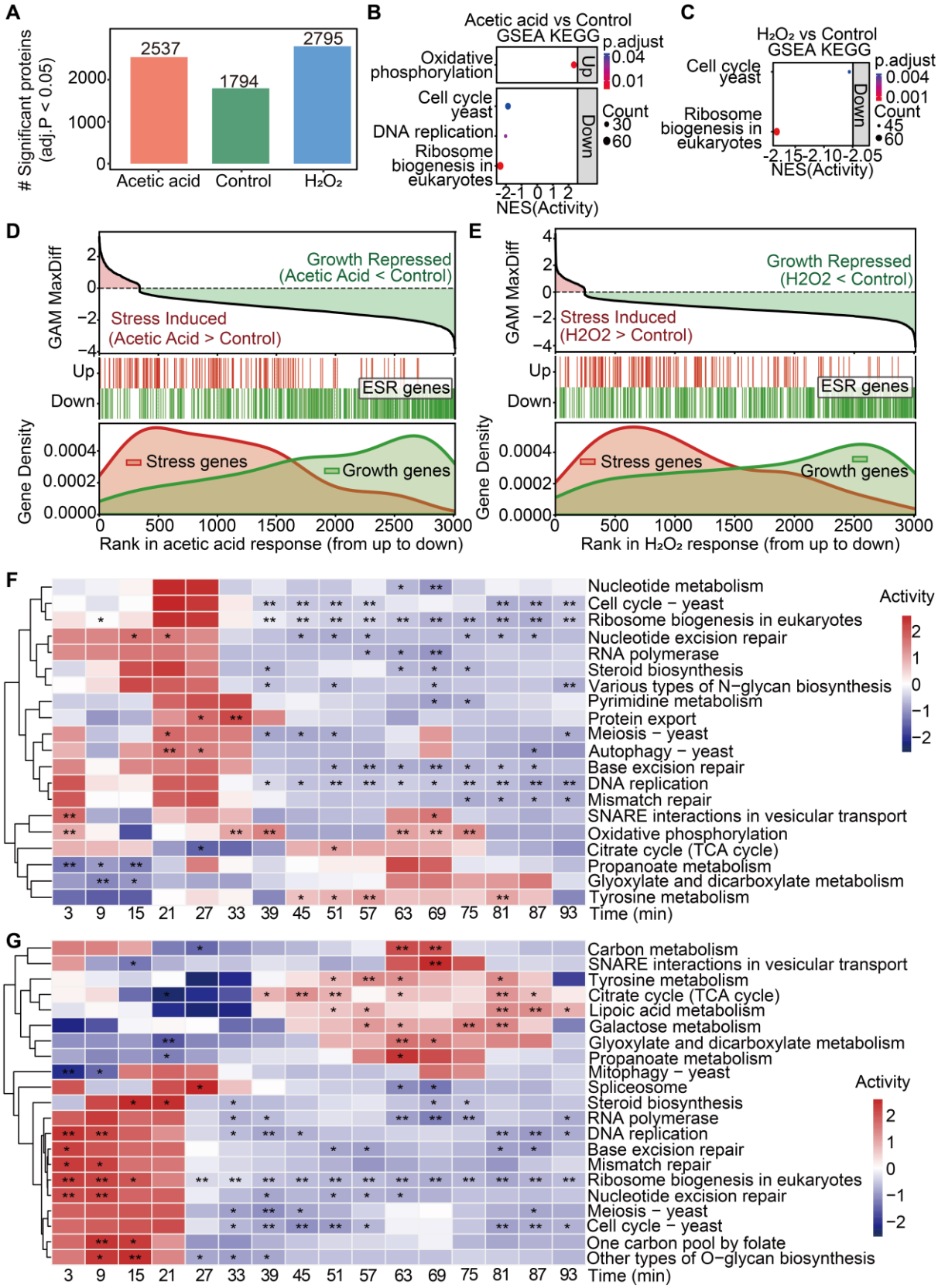

Extended Figure 4 | Global quantification, benchmark validation, and comprehensive time-resolved functional landscapes. (A) Summary of Generalized Additive Model (GAM) statistics. The

bar chart displays the number of proteins showing significant temporal abundance changes (adjusted $P < 0.05$). Notably, 1,794 proteins exhibit significant non-linear fluctuations even under control conditions ("Control baseline trend"), highlighting the necessity of dynamic background modeling. **(B, C)** Static Gene Set Enrichment Analysis (GSEA). Proteins were ranked by their kinetic magnitude (MaxDiff). **(B)** Acetic acid stress specifically induces oxidative phosphorylation while suppressing growth machinery. **(C)** H_2O_2 stress is dominated by the repression of cell cycle and ribosome biogenesis. **(D, E)** Validation of the "MaxDiff" kinetic metric against canonical Environmental Stress Response (ESR) benchmarks. The plots overlay the distribution of MaxDiff values (top curves) with the density of known ESR-induced (red) and ESR-repressed (green) genes. The strict segregation of stress genes to positive MaxDiff values and growth genes to negative values confirms that the kinetic metric accurately captures the polarity of the biological response for both (D) Acetic Acid and (E) H_2O_2. **(F, G)** Comprehensive time-resolved functional landscapes. Unlike the selected highlights in Main Figure 3, these heatmaps display the complete temporal evolution of all significantly enriched KEGG pathways (based on GAM-derived binned AUC scores across 16 time windows). **(F)** The acetic acid landscape visualizes the full metabolic exhaustion program, showing the interplay between early basal transcription/OxPhos activation and broad metabolic suppression. **(G)** The H_2O_2 landscape details the genomic triage strategy. Note that the positive enrichment (red) of central metabolic pathways (e.g., Citrate cycle, Carbon metabolism) implies relative preservation rather than absolute upregulation. Amidst the global proteomic downregulation triggered by H_2O_2, core metabolic enzymes exhibit significantly higher robustness (smaller decline) compared to the rapidly collapsing translation machinery, reflecting a cellular strategy to prioritize bioenergetic maintenance over growth during lethal stress.

Extended Figure 5

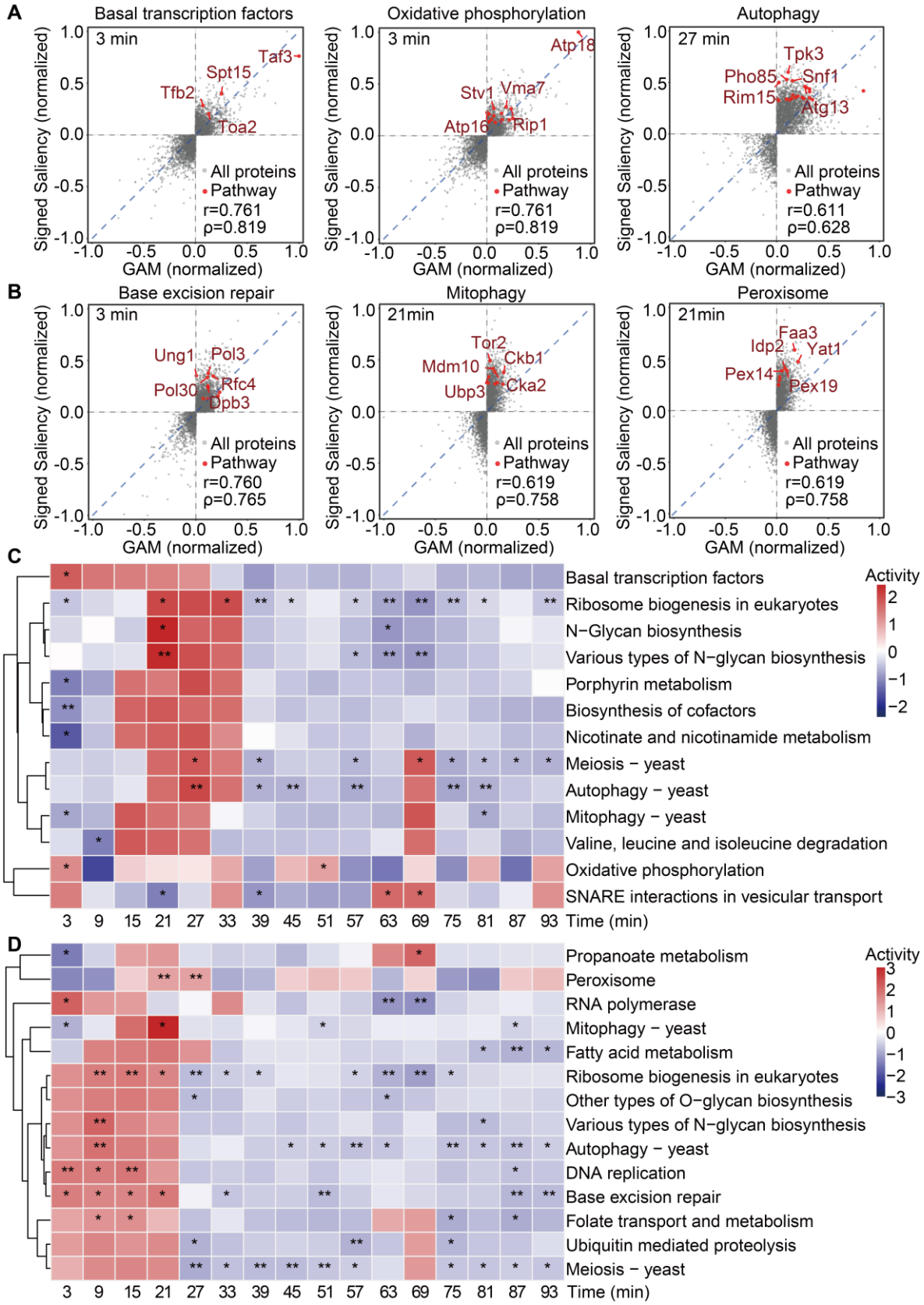

Extended Figure 5 | Decoupling of predictive importance from abundance changes and global gradient-based functional landscapes. (A, B) Scatter plots comparing model-inferred regulatory

importance (y-axis, normalized Signed Saliency) versus protein abundance changes (x-axis, normalized GAM fit) for representative pathways at specific time points. Both metrics are min-max normalized to the range [-1, 1]. Red points denote all proteins belonging to the indicated GSEA-enriched pathway, while grey points represent all the identified proteins. Specific labels indicate the top 5 proteins ranked by enrichment score (or all members for small sets, e.g., Basal transcription factors). **(A)** In the Acetic Acid condition (3 min), Basal transcription factors (top left) exhibit high positive saliency despite relatively small abundance changes, identifying them as early regulatory drivers that precede proteomic remodeling. Conversely, Oxidative phosphorylation (top middle) shows concordance between high abundance and high importance. **(B)** In the H_2O_2 condition, the critical 21-minute window reveals that proteins involved in Mitophagy and Peroxisome maintenance (e.g., Cka2, Idp2) possess high predictive importance relative to their abundance fold-changes, distinguishing them as key transient drivers. **(C, D)** Comprehensive time-resolved landscapes of pathway driver activity. Heatmaps visualize the temporal evolution of Signed Saliency scores for all significantly enriched pathways in (C) Acetic Acid and (D) H_2O_2 conditions. This gradient-based analysis complements the abundance-based profiles **(Extended Fig. 4)** by highlighting the active regulatory forces—such as the early initiation by Basal TFs (Acetic Acid) or the transient 21-minute pulse of organelle quality control (H_2O_2)—that drive the system's trajectory.